

**NAVAL POSTGRADUATE SCHOOL  
MONTEREY, CALIFORNIA**



**THESIS**

**AN EXAMINATION OF TWO SYNTHETIC  
APERTURE RADAR WIND RETRIEVAL  
MODELS DURING NORCSEX '95**

by

James Brian Hart

December, 1996

Thesis Co-Advisors:

Kenneth L. Davidson

Carlyle H. Wash

**Approved for public release; distribution is unlimited.**

19970618 102

# REPORT DOCUMENTATION PAGE

Form Approved OMB No. 0704-0188

Public reporting burden for this collection of information is estimated to average 1 hour per response, including the time for reviewing instruction, searching existing data sources, gathering and maintaining the data needed, and completing and reviewing the collection of information. Send comments regarding this burden estimate or any other aspect of this collection of information, including suggestions for reducing this burden, to Washington Headquarters Services, Directorate for Information Operations and Reports, 1215 Jefferson Davis Highway, Suite 1204, Arlington, VA 22202-4302, and to the Office of Management and Budget, Paperwork Reduction Project (0704-0188) Washington DC 20503.

1. AGENCY USE ONLY <i>(Leave blank)</i>	2. REPORT DATE December, 1996	3. REPORT TYPE AND DATES COVERED Master's Thesis	
4. TITLE AND SUBTITLE AN EXAMINATION OF TWO SYNTHETIC APERTURE RADAR WIND RETRIEVAL MODELS DURING NORCSEX '95			5. FUNDING NUMBERS
6. AUTHOR(S) James Brian Hart			8. PERFORMING ORGANIZATION REPORT NUMBER
7. PERFORMING ORGANIZATION NAME(S) AND ADDRESS(ES) Naval Postgraduate School Monterey CA 93943-5000			
9. SPONSORING/MONITORING AGENCY NAME(S) AND ADDRESS(ES)			10. SPONSORING/MONITORING AGENCY REPORT NUMBER
11. SUPPLEMENTARY NOTES The views expressed in this thesis are those of the author and do not reflect the official policy or position of the Department of Defense or the U.S. Government.			
12a. DISTRIBUTION/AVAILABILITY STATEMENT Approved for public release; distribution is unlimited.			12b. DISTRIBUTION CODE
13. ABSTRACT <i>(maximum 200 words)</i> <p>Synthetic Aperture Radar wind retrieval models have great potential to accurately depict the mesoscale wind field on the order of hundreds of meters. However, there are still significant hurdles to overcome in applying the theory in a fully automated algorithm. This thesis is a result of collaboration between the Nansen Environmental and Remote Sensing Center, Bergen, Norway and the Naval Postgraduate School. It examines two wind retrieval models on basis of in-situ and remote data from NORCSEX '95 in the interest of improving our understanding and application of these models. The individual models are based on Bragg backscatter from the ocean surface however, the CMOD4 model is directly related to the backscatter while the SWA model is related to the spectral resolution of the backscatter field. Each model has specific advantages and disadvantages related to processing and automation. For this data set they show very good agreement with each other and with in-situ measurements. Plots of optimum wind vectors derived from a combination of CMOD4 and SWA wind vectors are shown to illustrate the high resolution wind fields available with this technology.</p>			
14. SUBJECT TERMS Synthetic Aperture Radar, CMOD4, SWA, NORCSEX '95, ERS, Mesoscale Wind Fields			15. NUMBER OF PAGES 85
			16. PRICE CODE
17. SECURITY CLASSIFICATION OF REPORT Unclassified	18. SECURITY CLASSIFICATION OF THIS PAGE Unclassified	19. SECURITY CLASSIFICATION OF ABSTRACT Unclassified	20. LIMITATION OF ABSTRACT UL



Approved for public release; distribution is unlimited.

**AN EXAMINATION OF TWO SYNTHETIC APERTURE RADAR WIND  
RETRIEVAL MODELS DURING NORCSEX '95**

James Brian Hart  
Lieutenant Commander, United States Navy  
B.S., United States Naval Academy, 1983

Submitted in partial fulfillment  
of the requirements for the degree of

**MASTER OF SCIENCE IN METEOROLOGY AND  
PHYSICAL OCEANOGRAPHY**

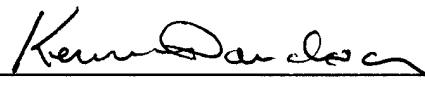
from the

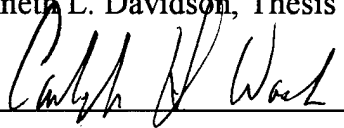
**NAVAL POSTGRADUATE SCHOOL  
December 1996**

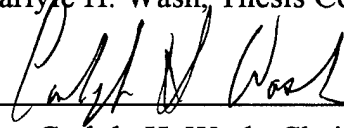
Author: \_\_\_\_\_

  
James Brian Hart

Approved by: \_\_\_\_\_

  
Kenneth L. Davidson, Thesis Co-Advisor

  
Carlyle H. Wash, Thesis Co-Advisor

  
Carlyle H. Wash, Chairman  
Department of Meteorology



## ABSTRACT

Synthetic Aperture Radar wind retrieval models have great potential to accurately depict the mesoscale wind field on the order of hundreds of meters. However, there are still significant hurdles to overcome in applying the theory in a fully automated algorithm. This thesis is a result of collaboration between the Nansen Environmental and Remote Sensing Center, Bergen, Norway and the Naval Postgraduate School. It examines two wind retrieval models on basis of in-situ and remote data from NORCSEX '95 in the interest of improving our understanding and application of these models. The individual models are based on Bragg backscatter from the ocean surface however, the CMOD4 model is directly related to the backscatter while the SWA model is related to the spectral resolution of the backscatter field. Each model has specific advantages and disadvantages related to processing and automation. For this data set they show very good agreement with each other and with in-situ measurements. Plots of optimum wind vectors derived from a combination of CMOD4 and SWA wind vectors are shown to illustrate the high resolution wind fields available with this technology.



## TABLE OF CONTENTS

I. INTRODUCTION .....	1
II. BACKGROUND .....	3
A. SYNTHETIC APERTURE RADAR .....	3
1. Principles .....	3
2. Importance of Ocean Long Waves on SAR Data .....	5
B. NORCSEX 95 .....	7
1. General .....	7
2. Platforms and Instruments .....	8
III. WIND FIELD RETRIEVAL TECHNIQUES .....	21
A. GENERAL .....	21
1. Range Spreading Loss .....	21
2. The Antenna Pattern .....	22
3. ADC Conversion Loss .....	22
B. THE CMOD4 MODEL .....	23
1. Thermal Stratification in the Atmospheric Boundary Layer .....	23
2. Wind Direction from CMOD4 .....	25
C. SAR WIND ALGORITHM .....	25
IV. OBSERVATIONS .....	35
A. GENERAL .....	35



B. 16 AND 17 SEPTEMBER 1995 .....	35
1. Atmospheric Synoptic Scale .....	35
2. Atmospheric Mesoscale .....	36
3. CMOD4 and SWA Results vs. In-situ Data .....	37
C. 23 SEPTEMBER 1995 .....	39
D. 27 SEPTEMBER 1995 .....	40
V. CONCLUSIONS AND RECOMMENDATIONS .....	69
LISTS OF REFERENCES .....	71
INITIAL DISTRIBUTION LIST .....	73

## ACKNOWLEDGMENTS

The author would like to extend his thanks for support and guidance to Professors Davidson and Wash in the preparation of this thesis. I also extend my thanks to persons in the Department of Meteorology Boundary Layer Studies Group who were involved in data collection during NORCSEX '95 and post-experiment data analysis: Keith Jones, Paul Fredrickson, and Tamar Neta. Persons at the Nansen Environmental and Remote Sensing Center (NERSC) in Solheimsvik, Norway provided invaluable support during the thesis as well as in the data collection; in particular Erik Korsbakken. Special acknowledgment is given to the Captain and crew of the R/V *Hakon Mosby* and to the Chief Scientists, Dr. Johnny Johannessen and Professor Ola Johannessen. NPS shipboard measurements in NORCSEX '95 were funded by NRaD, San Diego, CA as part of the "Remote Sensing of Marine Atmospheric Properties" project, and buoy measurements were funded by the NRL-TOWS, Stennis Space Center, MS as part of the "Evaluation of Buoy Motion/Orientation Measurements" project. Finally I would like to thank my wife Julie and our children for their constant support.

## I. INTRODUCTION

The capability to sense remotely the surface wind field over the ocean at a resolution on the order of hundreds of meters would be of great value to Naval and civilian meteorologists, especially in coastal areas. Scatterometers employed on spacecraft are limited in resolution to about 50 km. It is not practical to improve this resolution since it would require a much larger antenna. This physical limitation on antennae size can be relaxed by creating a synthetic aperture through analysis of the frequency shift of the transmitted signal. SEASAT in 1978 carried the first operational spacecraft-based Synthetic Aperture Radar (SAR), which was able to resolve images of about 25 m. The goal of the SEASAT SAR was to obtain high resolution images of the sea surface and sea ice. Operationally, it had limited coverage in the Northern Hemisphere and no coverage in the Southern Hemisphere because there was no on-board storage for the high data rate SAR which required direct real time transmission to the four ground stations equipped to receive it. The SEASAT SAR far exceeded its goals for providing high resolution images of ocean waves, internal waves, underwater topography, eddies, fronts, natural slicks and oil slicks (Beal *et al.* 1981, Allan ed. 1983).

Analysis of the surface wind was not one of the original/primary goals of the SEASAT SAR but one that evolved once the images became available. Wind fronts were clearly evident in many coastal SAR images where the scatterometer showed a smooth field or was degraded due to interference from the land backscatter (Allan ed. 1983). Subsequent SAR's have been employed on the Space Shuttle, ERS-1, ERS-2, and RADARSAT and have been used to

analyze the surface wind. However, the exact relationship between the SAR return and the ocean wave field is still not completely understood leading to errors in the processed wind fields.

The Norwegian Coastal Shelf Experiments (NORCSEX), located off the southwest coast of Norway, have been conducted since 1991 in support of the European Space Agency's European Remote Sensing (ERS) program. The most recent of these, NORCSEX '95, was conducted during the ERS-2 calibration trials. It collected in-situ data from the research vessel (R/V) *Hakon Mosby*, and from an instrumented buoy while both the ERS-1 and ERS-2 SAR's imaged the same area. This thesis is a result of collaboration between the Nansen Environmental and Remote Sensing Center, Bergen, Norway, and the Naval Postgraduate school. The Naval Postgraduate School's participation was to obtain high quality in-situ wind data for comparison. It examines two SAR wind models vs. the in-situ wind field with the goal of improving our knowledge of the errors in wind retrieval techniques. First, background descriptions of SAR and NORCSEX '95 are given in Chapter II. Descriptions of the wind retrieval models are presented in Chapter III. The results are presented in Chapter IV, and conclusions and recommendations for further study in Chapter V completes the thesis.

## II. BACKGROUND

### A. SYNTHETIC APERTURE RADAR

#### 1. Principles

The principles behind the operation of synthetic aperture radar are basically the same as those of any imaging radar with the exception of the synthetic aperture of course. It is not within the scope of this thesis to go into all the details of SAR operation and processing. However, the operation of a standard imaging radar will be reviewed and then the formation of the synthetic aperture and problems associated with SAR interpretation will be discussed.

The typical radar uses a pulse of microwave radiation to illuminate an object and measures the strength of the returned signal and the elapsed time, which are then processed and recorded for display and analysis. The factors affecting the image resolution are the pulse width, frequency, range to target, and the aperture or antenna size. When the radar is moving with respect to the target, as is the case with satellite imaging radars, then the pulse width determines the resolution in the range (cross track) direction and the aperture size determines the resolution in the azimuth (along track) direction. A typical geometry for a satellite based SAR is shown below in Figure 2.1.

Any radar using the same aperture for both transmitting and receiving has an angular resolution ( $\phi$ ) which is dependent upon its aperture length ( $L$ ) expressed in wavelengths.

$$\phi = 1/2L \quad (1)$$

To get higher resolution the aperture length is increased. Present scatterometer resolution is limited by its aperture (antenna) size to about 50 km. Doubling of the aperture (antenna) size of a satellite borne radar would be very expensive and would result in only a 25 km resolution. This physical limitation is overcome by the synthetic aperture radar which uses the spacecraft motion along an arc to create a large "synthetic aperture". The design image resolution of 30 m for the ERS-2 is achieved by transmitting a series of coherent pulses while the spacecraft travels the distance of the synthetic aperture. These pulses are then corrected for Doppler shift and processed to appear as one signal. The time it takes the spacecraft to travel the length of the synthetic aperture is only about 0.5 seconds. Fortunately this is much shorter than the period of the short gravity waves which SAR images so the error induced by this processing method is minimal.

In the case of a satellite-based SAR, such as ERS-2, the relationship between angular resolution ( $\phi$ ), slant range ( $h$ ), SAR wavelength ( $\lambda$ ), azimuthal resolution ( $r_a$ ), and aperture length is:

$$r_a = \phi * h / 2L \quad (2)$$

Much effort has gone into the interpretation of spacecraft SAR images since the first SEASAT images in 1978. It is generally accepted that the return signal over the ocean surface is due to Bragg scattering. The Bragg model states that the dominant backscattered energy will arise from the surface spectral components that resonate with the incident wave.

The ocean surface can be approximated by a series of planar facets each tangential to the

actual surface. The small scale roughness is superimposed on this on this surface so that the incident wave scatter has components due to the local slope (facet scattering), and the roughness (Bragg scattering). (Curlander and Mcdonough, 1991). The resultant backscatter curve is a function of incidence angle (Figure 2.2). From the Bragg theory, the optimal wavelength for imaging ocean waves is defined by the relationship:

$$\lambda_r/2 = \lambda \sin \theta, \quad (3)$$

where  $\lambda_r$  is the wavelength of the Bragg resonant wave. Using ERS-2 data this is approximately 5 cm which means that the waves being observed are the small surface gravity waves. Experiments have shown the strong correlation between the SAR return and the ocean wave field as well as the surface wind field for wind speeds greater than 3 m/s (Barrick and Peake 1968, Napolitano 1991 )

## **2. Importance of Ocean Long Waves on SAR Data**

It is believed that the ability of the SAR to detect ocean waves longer than the SAR wavelength depends on the modulation of the Bragg scatterers by these waves, although the exact relationship is not yet known. Since one of the wind models examined later is related to ocean long waves, a short review is useful. There are three principle mechanisms by which this modulation occurs: surface tilting, velocity bunching and hydrodynamic interactions (Alpers, Ross, and Rufenach, 1981).

### ***a. Surface Tilting***

Surface tilting results from the change in geometric presentation of the Bragg scatterers to the satellite. As depicted in Figure 2.3, the swell on which the Bragg waves are

superimposed changes the incidence angle and results in the tilt modulation phenomena. The radar backscatter is largest on the slope of the long swell wave directed toward the radar.

The magnitude of the tilt modulation transfer function (MTF) is dependent on both the viewing angle of the radar and the incidence angle of the long swell waves. It has been demonstrated that the range traveling long waves (waves traveling normal to the satellite) are likely to have an MTF about an order of magnitude larger than the azimuthally traveling waves (waves traveling in the same direction as the satellite) as seen in Figure 2.4 (Alpers et al 1981).

***b. Hydrodynamic Interactions***

The hydrodynamic interactions are complex interactions between waves and currents which result in increased short wave amplitudes and wavelengths near the crests of long waves (Figure 2.3). Although it is not well understood, Alpers and Hasselman (1978) used conservation of density in the wave interactions to develop a MTF which can be used for SAR processing. They also showed that the modulation due to hydrodynamic interactions was about half the magnitude of that due to tilt and that its maximum value was also for range traveling waves.

***c. Velocity Bunching***

Velocity bunching is the mechanism by which SAR can resolve waves that a standard imaging radar of the same resolution cannot. This is because the SAR uses Doppler shift to define the azimuth position of a target and any target motion will shift this position. The scattering elements on the ocean surface have a time varying radial velocity and their non-uniform azimuthal displacement results in wave-like patterns in the SAR images. This



mechanism also explains the appearance that ships are azimuthally offset from their tracks. If a wave is close to the range direction, the velocity bunching effects are small and linear. For waves traveling in the azimuthal direction, velocity bunching is the dominant modulation effect. There is only a small angular interval around the range direction where velocity bunching is a linear process and similar in magnitude to the tilt modulation (Figure 2.5). Alpers et al. (1981) discusses the three modulation mechanisms in detail and develops an MTF for the three that is valid in the fairly restricted conditions under which they can all be treated linearly.

The velocity bunching mechanism is the basis for the SWA wind model discussed in Chapter III. Since the SAR integration time is constant, the distortion increases with the wind speed, eventually limiting the azimuthal resolution of the SAR at a finite cut-off wavenumber. This cut-off wavenumber can then be related to the wind speed.

## **B. NORCSEX 95**

### **1. General**

NORCSEX '95 was conducted off the southwest coast of Norway over a twenty day period during September and October 1995. The third in the NORCSEX series, its' objectives were to improve our understanding of the SAR imaging mechanisms of marine boundary layer processes such as fronts, eddies, and winds in coastal areas. Researchers from several organizations participated in the exercise including: Nansen Environmental and Remote Sensing Center, Bergen, Norway; Canada Center for Remote Sensing, Canada; Naval Postgraduate School, Monterey, USA; Environmental Research Institute of Michigan (ERIM), Ann Arbor, USA; and the French Research Institute for Exploitation of the Sea

(IFREMER), Brest, France. During the twenty day period there were a total of 14 satellite passes (7 per satellite) over the NORCSEX '95 area. In-situ observations and data were collected on the R/V *Hakon Mosby* and a moored NPS buoy. The R/V *Hakon Mosby* attempted to stay in the SAR footprint and was used to collect data on features of particular interest in the SAR images in near real time.

## 2. Platforms and Instruments

### a. *R/V Hakon Mosby*

The University of Bergen operated the Research Vessel the R/V *Hakon Mosby* (Figure 2.7). It was instrumented and positioned to collect a variety of oceanographic and meteorological data within the SAR swath. The R/V *Hakon Mosby* left Bergen on 11 September and arrived in the vicinity of 58 deg 30 min N, 4 deg 45 min E. The first operations were to deploy current meter and the NPS instrumented meteorology buoy. The orbits of both ERS-1 and ERS-2 during this period were such that the R/V *Hakon Mosby* could transit to all ascending and descending SAR swaths off the South and Southwest Norwegian coasts during the period. No swath was duplicated.

The ocean surface and atmospheric conditions measured from the R/V *Hakon Mosby* that would be applicable to interpretation of SAR wind algorithms are SST, mean and turbulent wind, temperature and humidity, and mean pressure. The measured parameters on the R/V *Hakon Mosby* as well as on the NPS instrumented buoy are listed in Table 2.1. All airflow measurements were made from a mast that was set up on a platform attached to the ship's main mast. The height of these sensors ranges from 15.3 to 18.7 m and were well exposed except for ship relative winds clockwise from 160 to 200 degrees.

Mean vector wind was measured with both a propeller-vane and a sonic anemometer, while mean temperature and humidity were obtained with naturally aspirated sensors. Ships course and speed (determined from both ship a gyro/log system and from GPS positions) were used to derive true vector wind from measured apparent winds. This information was needed because of frequent ship course and speed changes required from oceanographic surveying. Mean SST was measured by an infrared thermometer mounted above the starboard bridge. All mean quantities were sampled at 1 second rates and stored at 5 second averages. Turbulent wind and temperature were obtained from the sonic anemometer, sampled at 21 Hz. Turbulent humidity was measured with a IR hygrometer. All shipboard fluctuating parameters were sampled at 21 Hz and stored without further processing for later analyses.

<b>Table 1: NORCSEX '95 Ship and Buoy Measurement Systems</b>		
	<b>Ship</b>	<b>Buoy</b>
Bulk Parameters (surface layer)		
Pressure	X	X
Vector Wind	X	X
Temperature (Air and Sea)	X	X
Humidity	X	X
Turbulence (surface layer)		
Vector Wind	X	X
Temperature	X	X
Humidity	X	X
Surface Waves		
Directional Wave Spectra		X
Vertical structure (MABL)		
Vector Wind	X	
Temperature	X	
Relative Humidity	X	

***b. NPS Instrumented Buoy***

An instrumented moored meteorological and surface wave buoy, Figure 2.6, was designed and constructed by NPS investigators especially for validation/calibration of active (radar) remote sensors. The special features of the buoy were its capability to measure surface layer wind, wind stress, thermal stability and 2-dimensional surface wave properties from swell to centimeter wavelengths. The buoy hull was a toroid, 2 m in diameter with a 5 m mast. The sensor and acquisition controls, mass memory storage, and batteries were housed in a cylindrical case (electronic case) mounted in the center of the toroid. The mooring chain and floatation design were sufficient to maintain

the buoy vertical under most wave conditions.

Mean atmospheric surface layer properties were measured with a propeller-vane anemometer, and natural aspirated temperature and relative humidity sensors mounted near the 3 m level on the mast. Mean sea surface temperature was obtained from a thermocouple imbedded at the bottom of the buoy cylindrical electronics case. Mean pressure was measured by a sensor mounted in the electronics case. The mean data were sampled at a 1 Hz rate and averaged and stored at 5-minute intervals.

Turbulent wind and temperature were measured with a 3-dimensional sonic anemometer mounted at the top of the mast, at the 5 m level. The surface wave conditions were measured with two separate systems. Wave conditions longer than the 2 m toroid diameter, were interpreted from a system with three orthogonal accelerometers and three rate gyros. The resulting 3-dimensional motion information, sampled at 10 Hz, was also used to remove buoy motion contamination of sonic anemometer sensed velocities. Shorter waves, corresponding to capillary scale waves, were measured with three vertically oriented wires, spaced 4 cm apart, that penetrated the interface about 1.5 meters upwind of the buoy. The turbulent and surface wave parameters were sampled at 10 Hz rates and stored directly onto the mass memory device for later time series analyses.

The buoy was deployed from the R/V *Hakon Mosby* at 58 deg 30 min N and 4 deg 45 min E on 18 September. The mooring location was on the line between two SAR swaths, projected for the NORCSEX '95 period. It is believed that the buoy and its instrumentation systems worked properly for the 2-day period when the SAR swaths were near enough for its data to be used as a surface truth. The complexity of the data analyses

limited its use for interpretations in this thesis. In particular, the merged buoy and sonic anemometer data analyses have not been developed enough to achieve full confidence in wind stress determination.

*c. ERS-2*

The ERS-2 satellite, launched in April 1995, is the second in a series designed primarily to provide high resolution information of the ocean environment. It is essentially the same as the ERS-1 with the exception of a number of enhancements and one new instrument designed to measure the chemical composition of the atmosphere (GOME). The other instruments carried by ERS-2 are the:

- Active Microwave Instrument (AMI),
- Radar Altimeter (RA),
- Along Track Scanning Radiometer (ATSR),
- Microwave Radiometer (MWR), and the
- Precise Range and Range Rate Instrument (PRARE).

The AMI incorporates the scatterometer and SAR and operates in three different modes to provide oceanic wind and wave measurements. The RA provides the precise altitude over all terrain. The ATSR measures sea surface temperatures and the ERS-2 version of this instrument has been enhanced by the addition of visible channels to monitor vegetation. The MWR and the PRARE are used to support the RA in determining the precise location of the satellite.

Both ERS satellites are in a sun synchronous orbit crossing the equator on the descending node at about 10:30 local time each day. The satellites are currently in a

35 day repeat orbit with a one day separation with ERS-1 in the lead. This arrangement provides an excellent opportunity to compare the results from the two satellites. The orbits of either satellite can be changed if needed but it is expected that they will remain in this tandem mode.

The instrument of interest in NORCSEX '95 is the AMI which incorporates the scatterometer and SAR and operates in three different modes to provide oceanic wind and wave measurements. It is the largest and uses the most power of all the instruments on board. The AMI has three modes of operation: scatterometer, SAR, and wave. The scatterometer mode can be used continuously and images a swath of 500 km on the sea surface. It provides wind speed and direction at a resolution of about 50 km and accuracies of 2 m/s and  $20^\circ$ . The SAR mode uses a C-band SAR to image a 100 km swath on the ocean surface. It consumes so much power that it can only be used for about ten minutes per orbit. The wave mode provides small images at 200 km intervals which are used to generate ocean-wave spectra, showing wave energy as a function of wavelength and direction.

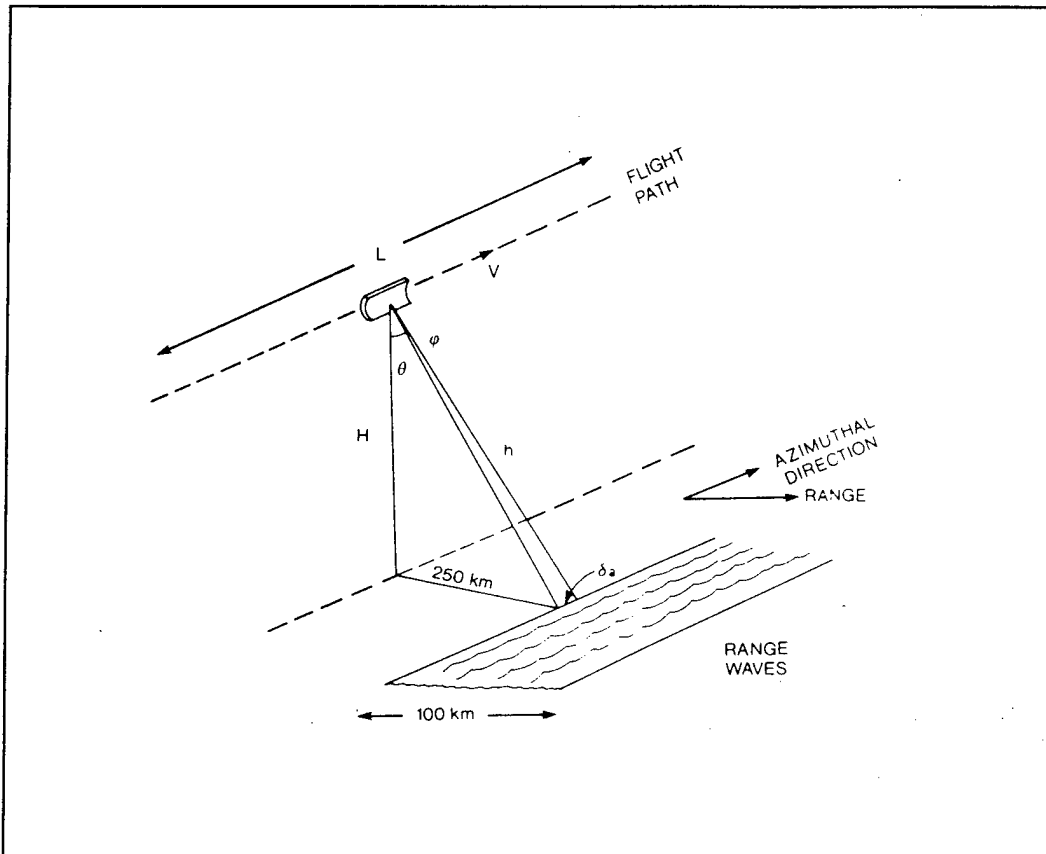
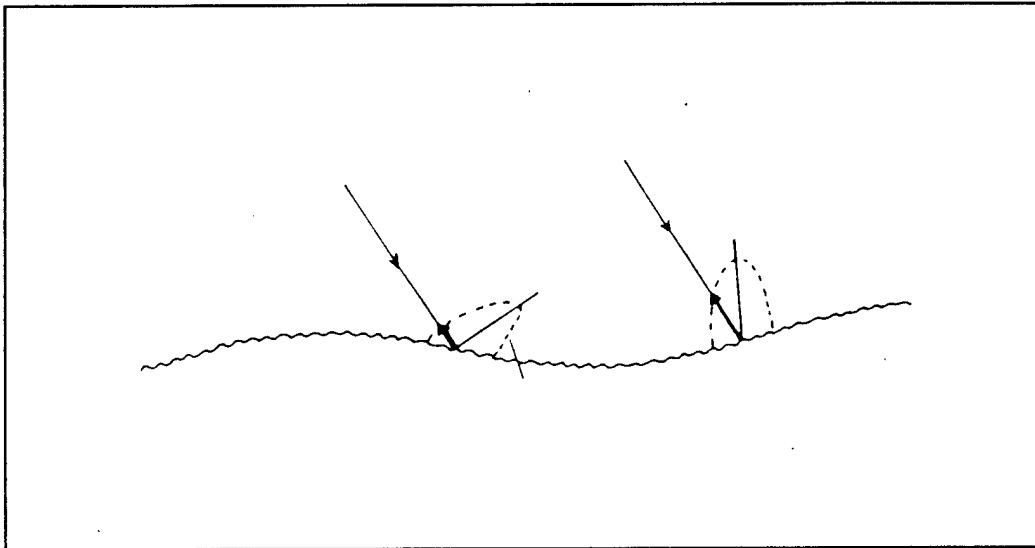


Figure 2.1 Typical Satellite SAR Geometry (from Allan ed. 1983).





**Figure 2.2** Bragg Scattering Geometry. Note the Most Preferential Location of Bragg Scatterers on the Larger Swell Wave Results in a Greater Backscatter Magnitude (as Indicated by the Magnitude of the Respective Reflected Signals) (after Curlander and Mcdonough, 1991)

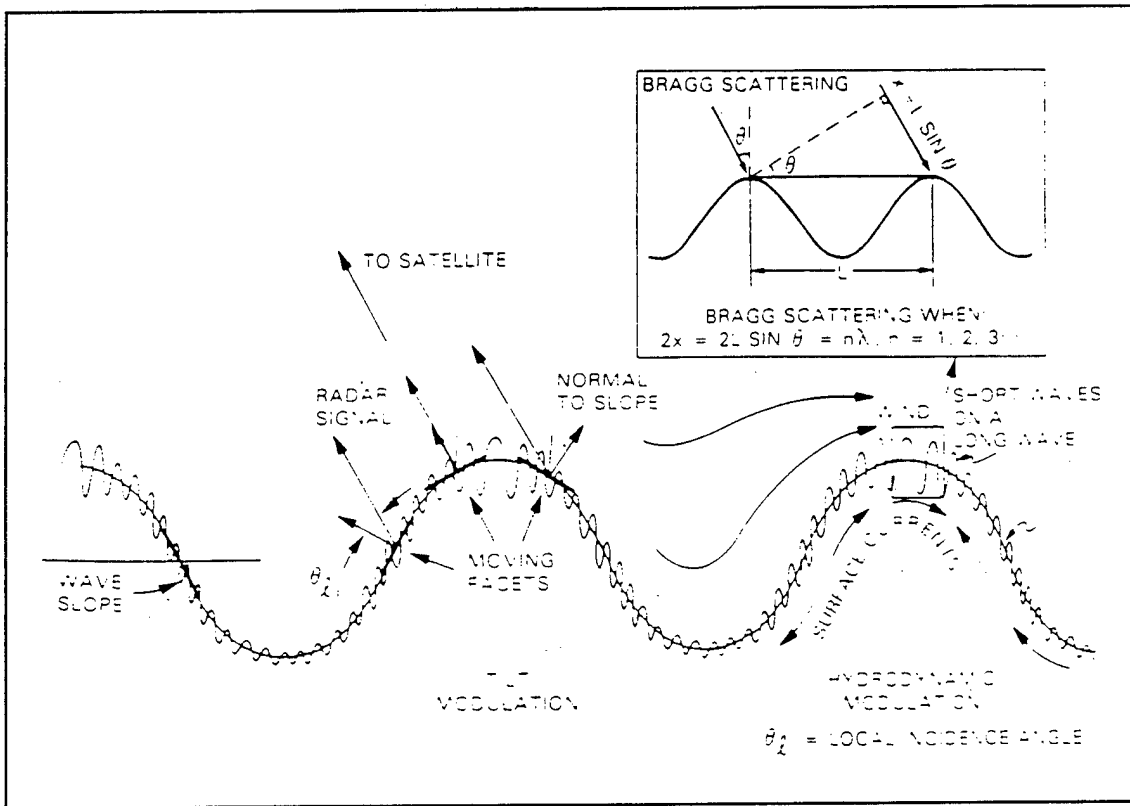
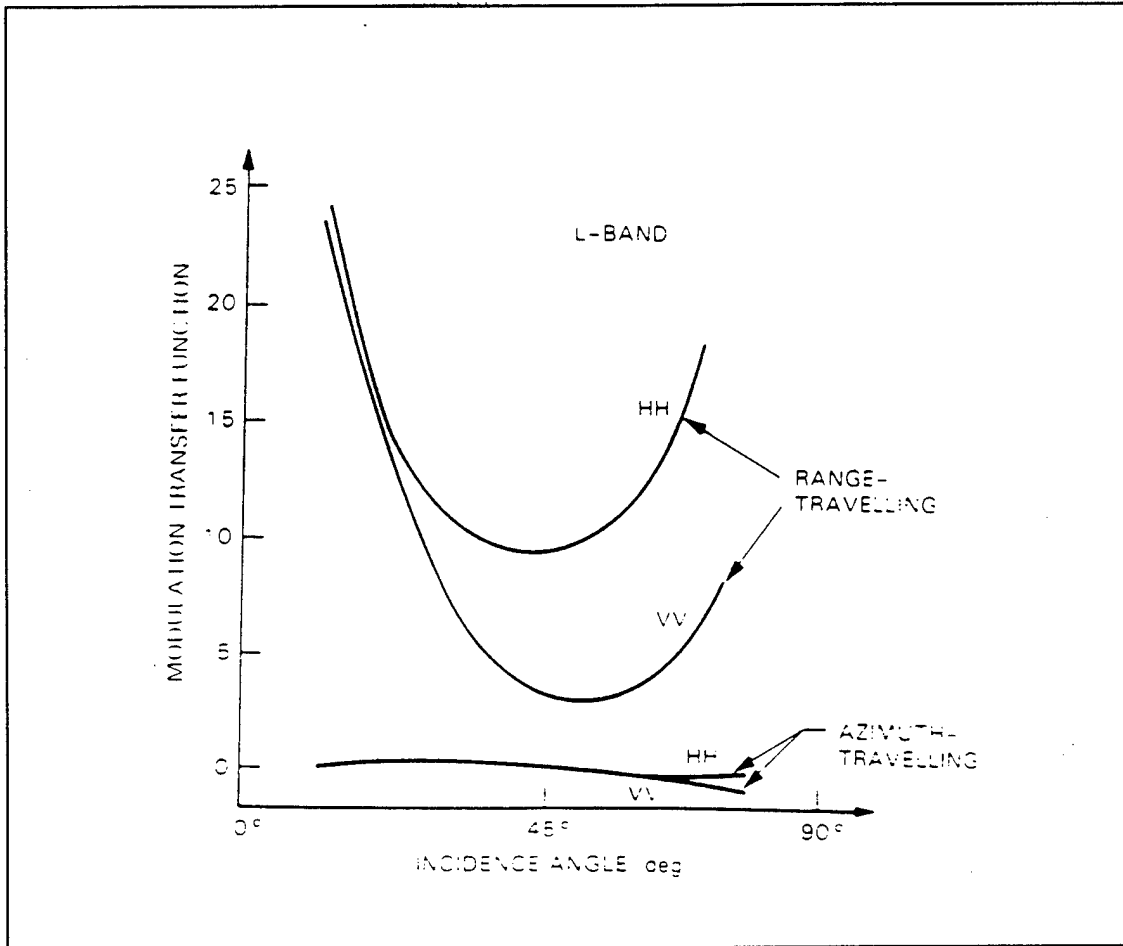
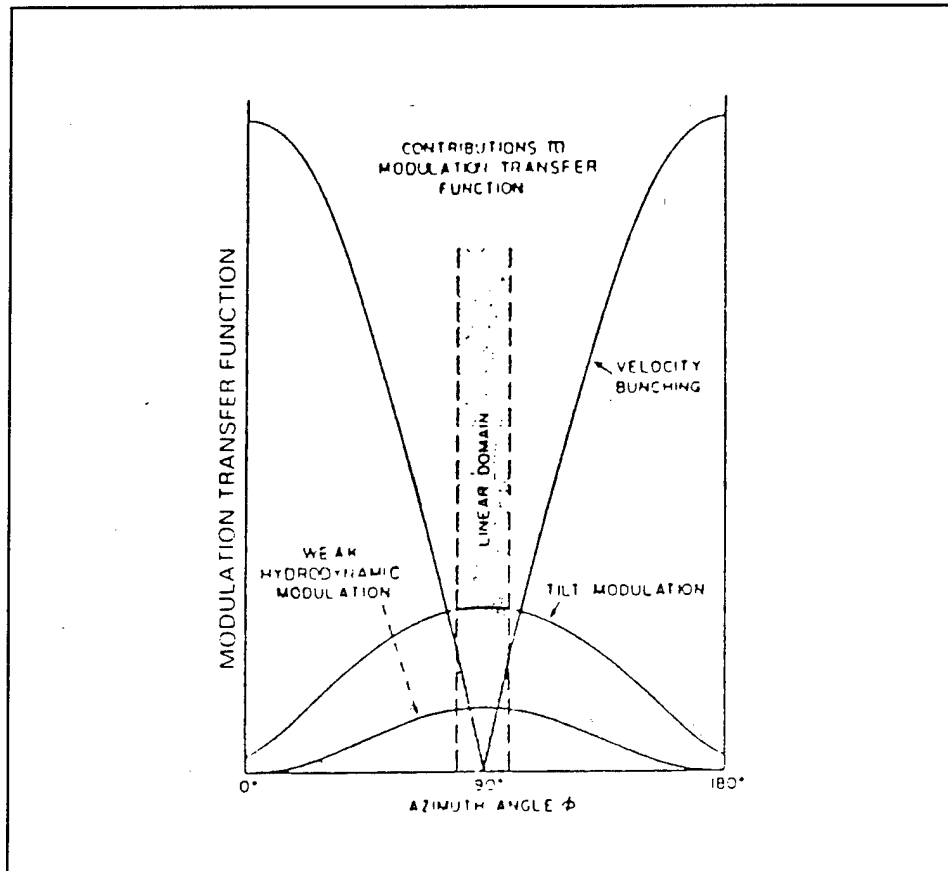


Figure 2.3 Sketch Illustrating Both the Tilt and Hydrodynamic Mechanism. (From Alpers *et al.* 1981)



**Figure 2.4** Modulation Transfer Function vs. Incidence Angle and Polarization. (from Alpers *et al.* 1981)



**Figure 2.5** The Dependence of the Modulation Transfer Function Describing Tilt, Hydrodynamic, and Velocity Bunching Modulation on Azimuthal Angle. There is a Small Angular Interval Around the Range Direction Where Velocity Bunching is a Linear Process. (From Alpers *et al.* 1981)

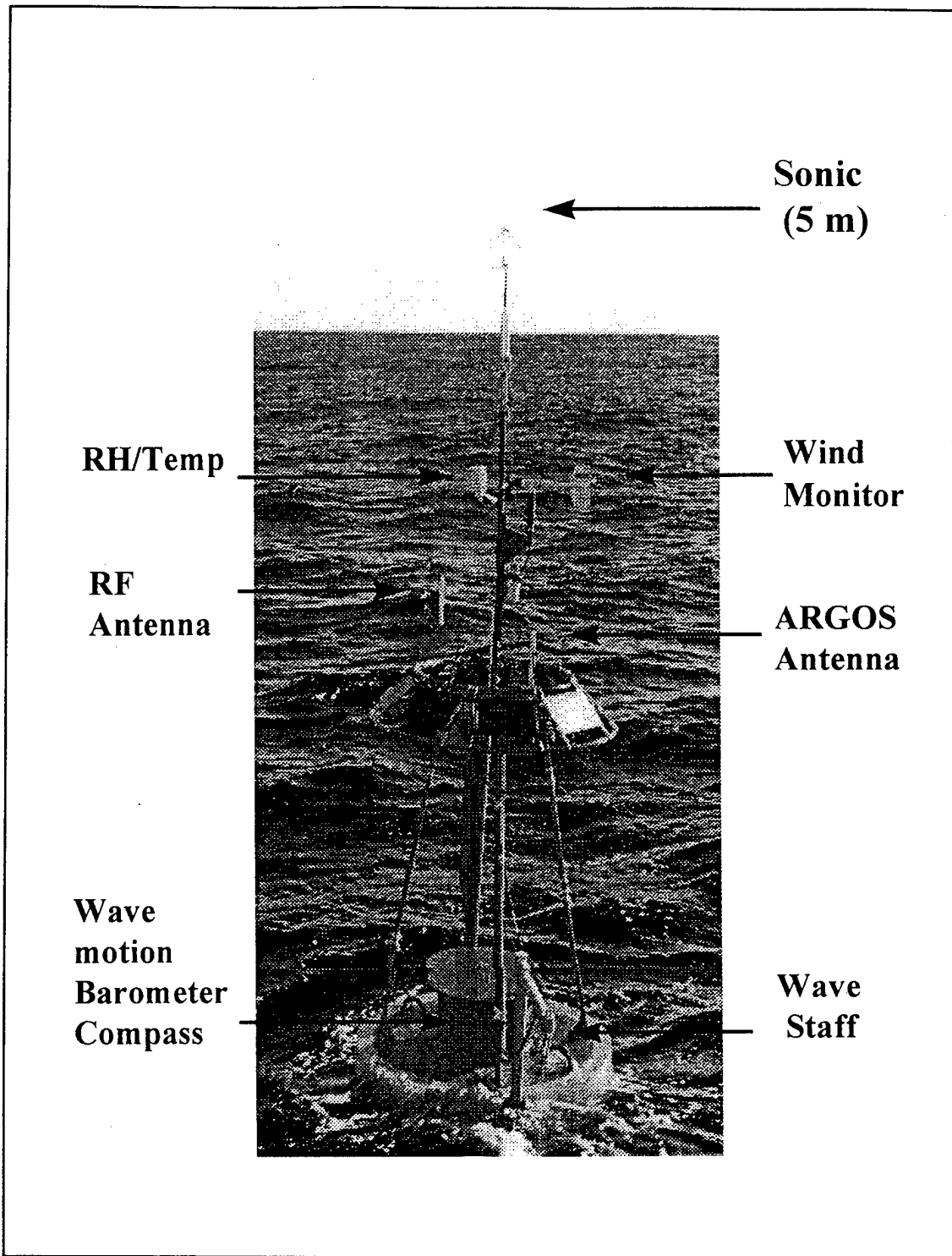


Figure 2.6 NPS Instrumented Buoy

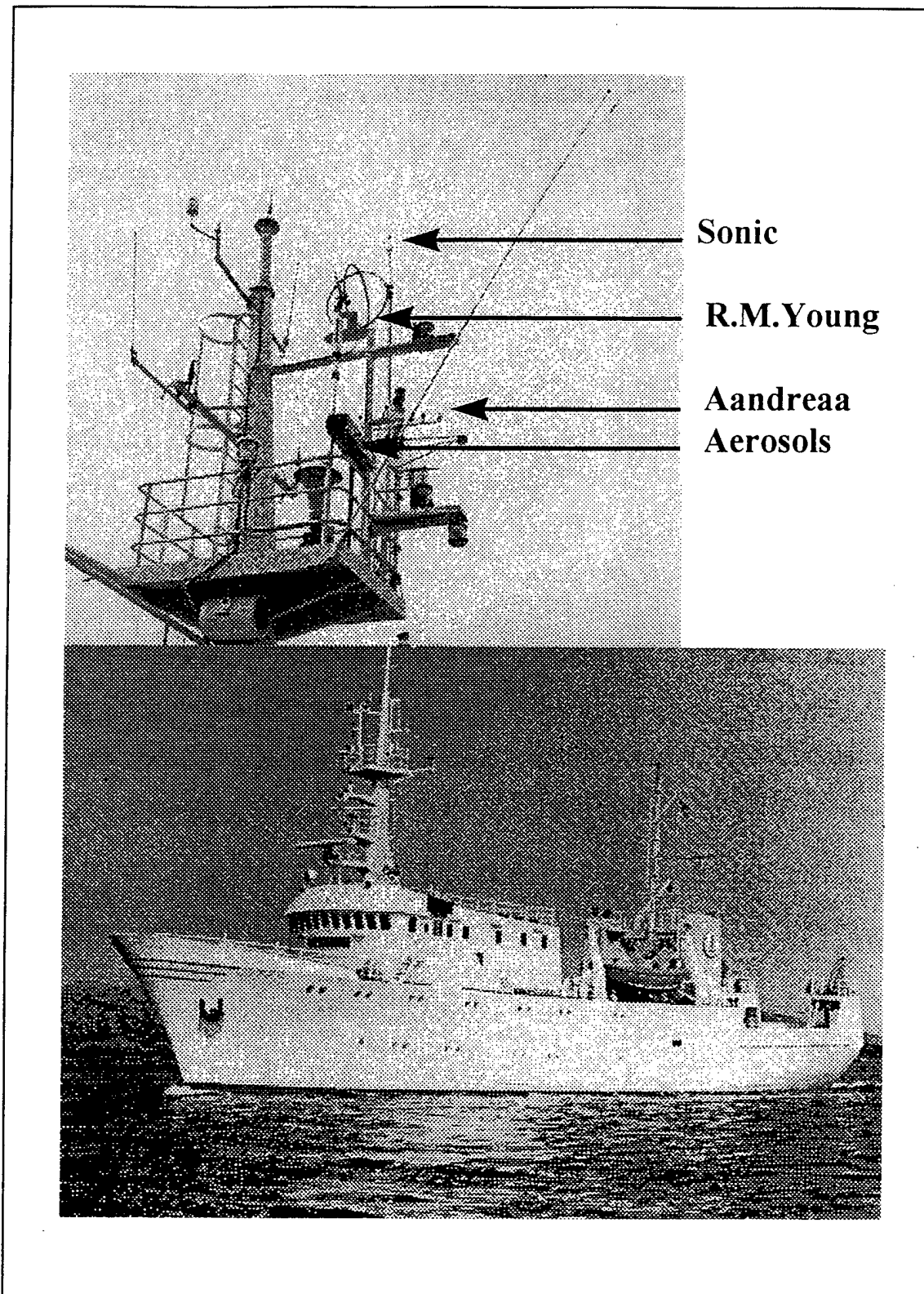


Figure 2.7 University of Bergen, Norway Research Vessel *Hakon Mosby*

### III. WIND FIELD RETRIEVAL TECHNIQUES

#### A. GENERAL

Although there are many SAR wind algorithms, this thesis is focused on the two applied by Korsbakken (1996) on ERS-1 and ERS-2 SAR data from NORCSEX '95. Specifically, these were the CMOD4 wind algorithm, and the SAR Wind Algorithm (SWA). The description of the two algorithms following Korsbakken (1996) follows.

In order to retrieve the absolute radar backscatter value ( $\sigma_0$ ), necessary to compute the wind field from the CMOD4 model, comprehensive calibration of the data is required, Scoon (1995). The calibration includes corrections for range spreading loss, for the antenna pattern, and for the power loss in analog to digital conversion (ADC). A brief description of these corrections is provided here to emphasize the importance of the calibration when using models which rely solely on the radar backscatter intensity. In extreme cases the values of  $\sigma_0$  are corrected more than 5 dB.

##### 1. Range Spreading Loss

The range spreading loss is the signal attenuation when the signal propagates from the radar to the target and back to the receiving antenna. The loss is expressed as:

$$\Omega_{(dB)} = 10\log\left(\frac{R^3}{R_{ref}^3}\right) \quad (4)$$

where  $R$  is the slant range distance to the target location and  $R_{ref}$  is the reference slant range distance at mid swath (approximately  $23^\circ$ ), Scoon (1995). The corrections for ERS-1 SAR

geometry lie within -0.3 dB in near range to 0.4 dB in far range.

## 2. The Antenna Pattern

The different sigma values have to be corrected for the change in the antenna gain as a function of the local incidence angle. The correction values are provided from antenna pattern functions estimated from data collected over homogeneous areas such as the Amazonian rain forest. The in-flight ERS SAR antenna pattern is computed from the Committee on Earth Observing Satellites header information. The antenna patterns are determined as a function of the slant range time to each pixel ( $\tau_n$ ) by a polynomial fit with five coefficients (Laur *et al.* 1993), given as:

$$A(\tau_n) = C_0 + C_1\tau_n + C_2\tau_n^1 + C_3\tau_n^2 + C_4\tau_n^3 + \tau_n^4 \quad (5)$$

## 3. ADC Conversion Loss

The saturation effect of ADC in the satellite is described in Laur *et al.* (1993), Scoon (1995), and Meadows and Willis (1995). The effect is strongest over the ocean in the near range and increases with radar back scatter intensity (i.e. at high winds). It leads to an underestimation of the radar back scatter. A curve which gives the correction is shown in Figure 3.1 (Willis 1995). Based on this sequence of corrections the expression for the calibrated  $\sigma_0$  becomes

$$\sigma_{0,cal} = (I)_{dB} - K_{dB} + \beta_{dB} + \Omega(\alpha)_{dB} + G(\alpha)_{dB} + PL_{dB} \quad (6)$$

where K is the calibration constant (scaling factor, typically 55 to 60 dB, this factor is dependent on the SAR processing),  $\beta = 10 \log(\sin \alpha / \sin \alpha_{ref})$ ,  $\Omega(\alpha)$  is the range spreading loss,  $G(\alpha)$  is the



antenna pattern correction and PL is the power loss due to ADC.

## **B. THE CMOD4 MODEL**

The CMOD4 wind retrieval model (Stofflen and Anderson, 1993) is developed for the ERS-1 scatterometer but it is also shown to give good estimates of wind speed (i.e. Vachon and Dobson, 1995; Vachon, Johannessen, and Brown, 1995; and Johannessen, Vachon, and Johannessen, 1995) when applied to ERS-1 SAR images. The model was developed for deep sea conditions. The CMOD4 gives a theoretical  $\sigma_0$  values a function of relative wind direction  $\phi$  (defined in Figure 3.2), and local incident angle ( $\alpha$ ) of the sub-area expressed as:

$$\sigma^0 = B_0[1 + B_1\cos(\phi) + B_2\cos(2\phi)] \quad (7)$$

The coefficients  $B_0$ ,  $B_1$ , and  $B_2$  depend on the radar beam incidence angle ( $\alpha$ ) and wind speed. The accuracy in the wind model is given to  $15^\circ$  in relative wind direction and 2 m/s in wind speed.

Figure 3.3 and Figure 3.4 show the radar backscatter sensitivity to incidence angles from  $19^\circ$  to  $26^\circ$  (typical range for ERS-1,2 SAR) and wind direction  $\phi = 0^\circ$  (up wind),  $\phi = 280^\circ$  (cross wind). Figure 3.5 shows a 3D solution surface for wind speeds ranging from 2 to 20 m/s and wind direction from  $0^\circ$  to  $360^\circ$  at an incidence angle equal to  $23^\circ$ . The  $180^\circ$  ambiguity of the wind direction is clearly manifested by the  $\cos(\phi) + \cos(2\phi)$  variation of the curve. For any wind speed the radar back scatter varies from a maximum for up-wind ( $0^\circ$ ) and down-wind ( $180^\circ$ ) to minimum for cross-wind ( $90^\circ$ ,  $270^\circ$ ).

### **1. Thermal Stratification in the Atmospheric Boundary Layer**

The thermal stratification is expressed by the air-sea temperature difference ( $\Delta T$ ) which

gives three possibilities:

$$\text{Unstable stratification:} \quad \Delta T < 0 \quad (T_{\text{sea}} > T_{\text{air}})$$

$$\text{Neutral stratification:} \quad \Delta T = 0 \quad (T_{\text{sea}} = T_{\text{air}})$$

$$\text{Stable stratification:} \quad \Delta T > 0 \quad (T_{\text{sea}} < T_{\text{air}})$$

The CMOD4 model is derived for a neutral stratification. The CMOD4 derived wind speed must be modified in order to compute the wind speed ( $U_{10}$ ) from the radar back scatter accounting for the stratification ( $\Delta T$ ) in the atmospheric boundary layer. The modification can be derived from expressions relating unstable (unst.) and stable (st.) stratification to neutral (neut.) stratification as suggested by Wu (1993):

$$\text{Unstable cases:} \quad \frac{C_{s,unst}}{C_{10,neut}} = \exp(0.614(-\Delta T/U_{10})^{5/3}) \quad (8)$$

$$\text{Stable cases:} \quad \frac{C_{s,st}}{C_{10,neut}} = \exp(0.424(0.614)(-\Delta T/U_{10})^{5/3}) \quad (9)$$

Here C is the drag coefficient that is a function of the stratification and can be expressed as:

$$\begin{aligned} C_{10,unst} &= \tau/\rho(U_{10,unst})^2 \\ C_{10,neut} &= \tau/\rho(U_{10,neut})^2 \\ C_{10,st} &= \tau/\rho(U_{10,st})^2 \end{aligned} \quad (10)$$

where  $\rho$  is the density of the air and  $\tau$  is the surface stress.

Considering the schematic in Figure 3-6, the surface stress and corresponding radar backscatter can be assumed constant while the wind speed at 10 m can be represented by three

different values associated with the stratification as obtained from equation 8, 9 or 10.

Figure 3.7 shows the  $U_{10}$  corrected wind speed as a function of  $\Delta T$  for different  $U_{10}$  neutral wind speeds. These curves can be used as a first order correction to the derived CMOD4 wind speed results when the stratification differs from the neutral situation. It is important to have an in-situ data set that includes the necessary data to make the stability correction.

## 2. Wind Direction from CMOD4

The wind direction can also be estimated from the CMOD4 model for different incidence angles provided the wind speed, derived from the SWA method, can be associated with the corresponding measured radar backscatter ( $\sigma_0$ ) at the solution surface shown in Figure 3.5. In such cases four solutions, i.e. two pairs, each with a  $180^\circ$  ambiguity can be found, except in the cases when the direction is close up - or down wind, for which only one pair is found (Note that for the three beam scatterometer on ERS-1, 2 the number of solutions is reduced to a single pair with a  $180^\circ$  ambiguity).

It has been demonstrated (Johannessen *et al.* 1995) that wind streaks manifested in the SAR images can be used to indicate the near surface wind direction during the SAR integration time. In such cases the number of wind direction solution pairs are also reduced to one ( $180^\circ$  ambiguity).

## C. SAR WIND ALGORITHM

Imaging of the large scale properties of the ocean surface is a result of modulation of the surface roughness at scales approximately equal to the radar wavelength by the long waves. A restriction in the registration of the ocean wavelength is the azimuth smearing and the cut-off in the ocean wave number spectrum in the azimuth direction. The cause of the azimuth smearing

and cut-off is the “line of sight” (direction) component of the velocity of the azimuth traveling waves which leads to a Doppler shift in the reflected radar signal during the SAR integration time. This shift, in turn, leads to a displacement of the intensity of the SAR image during SAR processing. The result of the displacement is a smearing of the image intensity which significantly affects the spatial resolution of waves propagating in the azimuth direction.

The SAR Wind Algorithm (SWA) proposed by Chapron et. al. (1995 ) is an empirically derived relation for the estimation of wind speed. The relation is between the smearing effects in the SAR image, image statistics, and the wind field. Smearing effects tend to increase the coherence (correlation length) of the radar returns in the spatial image domain and influence on the SAR image statistics. The latter can be used to estimate the wind speed.

The empirical relation, based on evaluation of 1200 SAR wave-mode images with a central incidence angle of 20.2 is given by Chapron et. al. (1995 ) as

$$U_{10} = 4.75\sigma_I^2 \quad (11)$$

$$\lambda_c = 110\sigma_I^2 + 30 \quad (12)$$

$U_{10}$  is the wind speed at 10 m above the surface,  $\sigma_I$  is the variance of the intensity for the processed imaggettes  $\lambda_c$  and is the azimuthal cut-off wavelength. Combination of these two equations then yields:

$$U_{10} = 4.75 \frac{\lambda_c - 30}{110} \quad (13)$$

It is important to emphasize that equation 11 and 12 are only valid for the specific processing of the wave mode imagettes because of different gain factors and weighting used in the processing (i.e. the values in two different products may not be directly comparable).

Assuming a Gaussian shaped low pass filter for the azimuthal cut-off, the cut-off wavelength can be estimated from the auto covariance function (ACF) derived from an inversion of the SAR image power density spectrum (Wiener Khinchins theorem). As proposed by Chapron et al. (1995), the ACF can be regarded as a sum of the narrow peak due to spatial resolution and a broadened "shoulder" corresponding to the Gaussian shaped filter (in the spectral domain) defined as:

$$c(x) \cong \exp\left(-\frac{\pi^2 x^2}{\lambda_c^2}\right) \quad (14)$$

where  $x$  is the lag in the ACF. A Gaussian function  $f(x) = \exp(-ax)^2$  is then fitted to the ACF in the azimuth direction over the broadened "shoulder" part of the function. In return  $\lambda_c$  is then obtained from the relation  $f(x) = c(x)$ .

An example of a strong azimuth cut-off is shown in Figure 3.8 while an example where the azimuth cut-off is weak (broad spectral response in azimuth) is shown in Figure 3.9. The latter response lies near to the ACF of the system transfer function (i.e. the speckle spectrum).

The fit of the Gaussian function  $f(x)$  is obtained by a minimization of a costfunction representing the deviation between the estimated autocorrelation function  $c(x)$  and  $f(x)$ . The minimization is carried out iteratively, computing a new model state and its gradient from a new appropriated set of control parameters at each iteration step. The flow chart in Figure 3.10

summarizes the SWA computing steps.

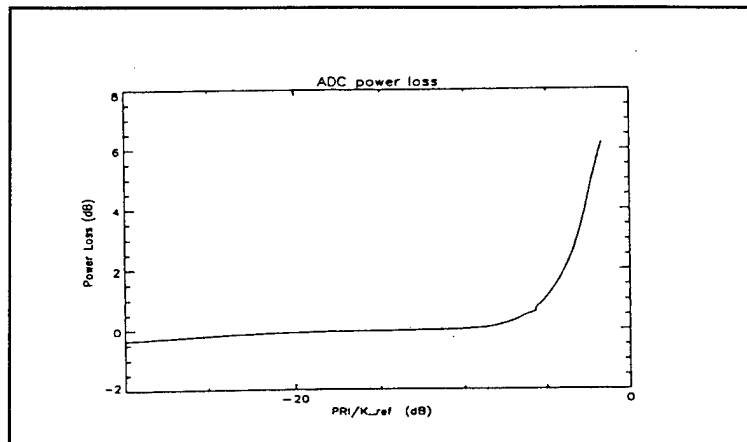


**Figure 3.1** The Curve for Deriving the Values for ADC Saturation Corrections. PRI/K\_ref is the “raw” (uncalibrated) SAR image intensity

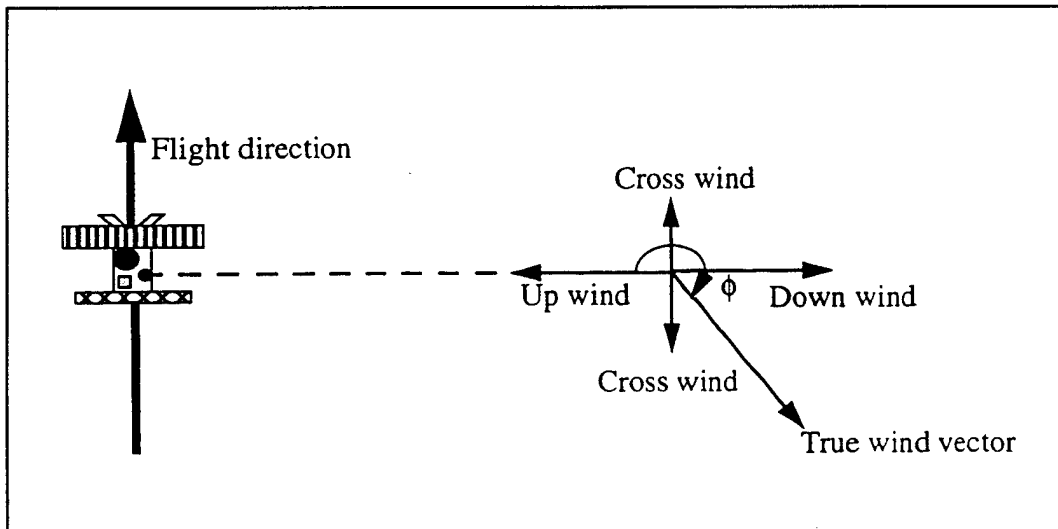


**Figure 3.2** Definition of Terms and Relative Wind Direction Relative to “true” Wind Direction vs. Satellite Flight Direction (Azimuth).

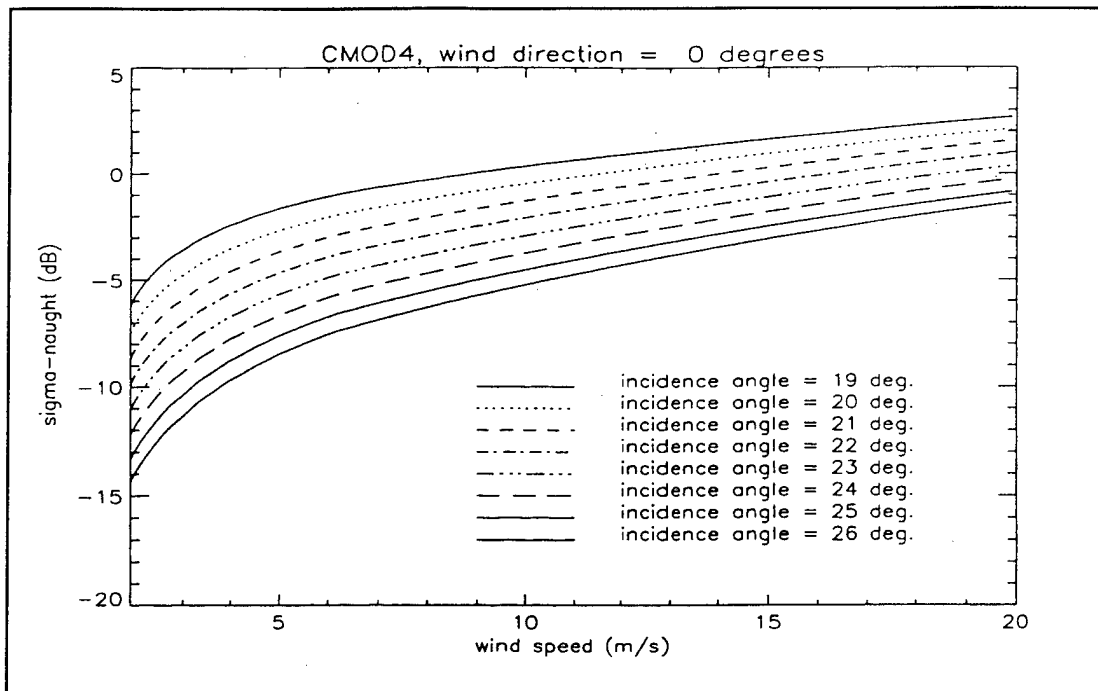


**Figure 3.3** Predicted Radar Backscatter Values vs. Wind Speed for Incident Angles Ranging from 19° to 26° and a Relative Wind Direction of 0°.

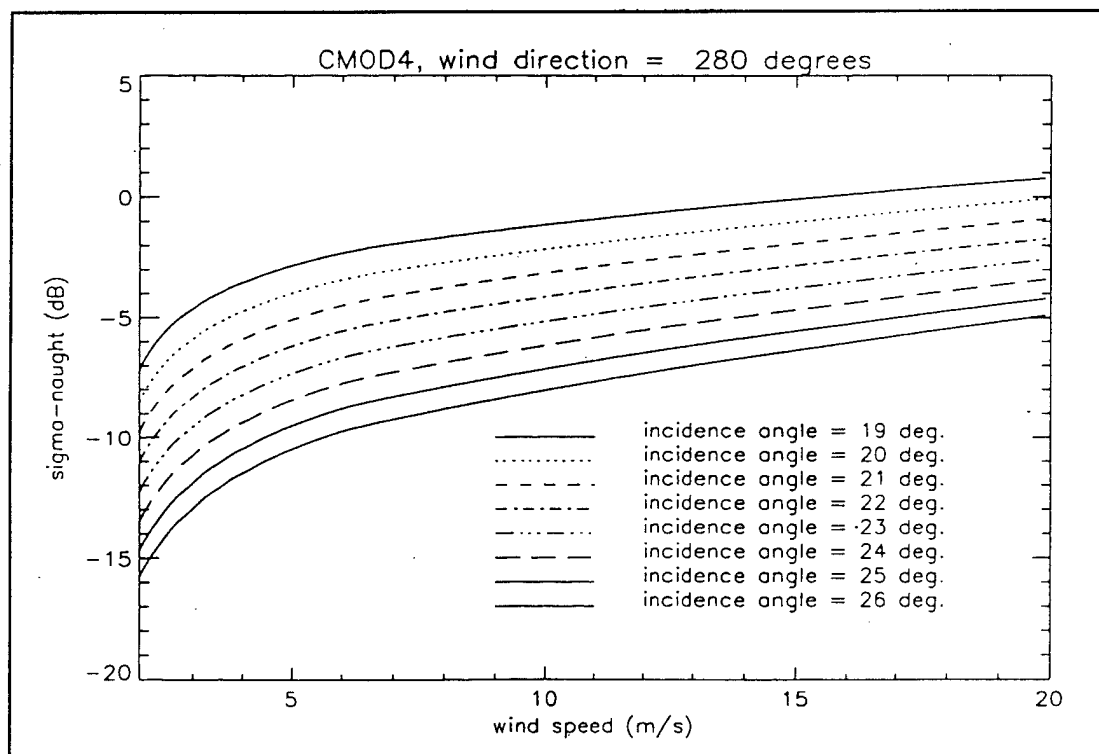


**Figure 3.4** Predicted Radar Backscatter Values vs. Wind Speed for Incident Angles Ranging from 19° to 26° and a Relative Wind Direction of 280°.



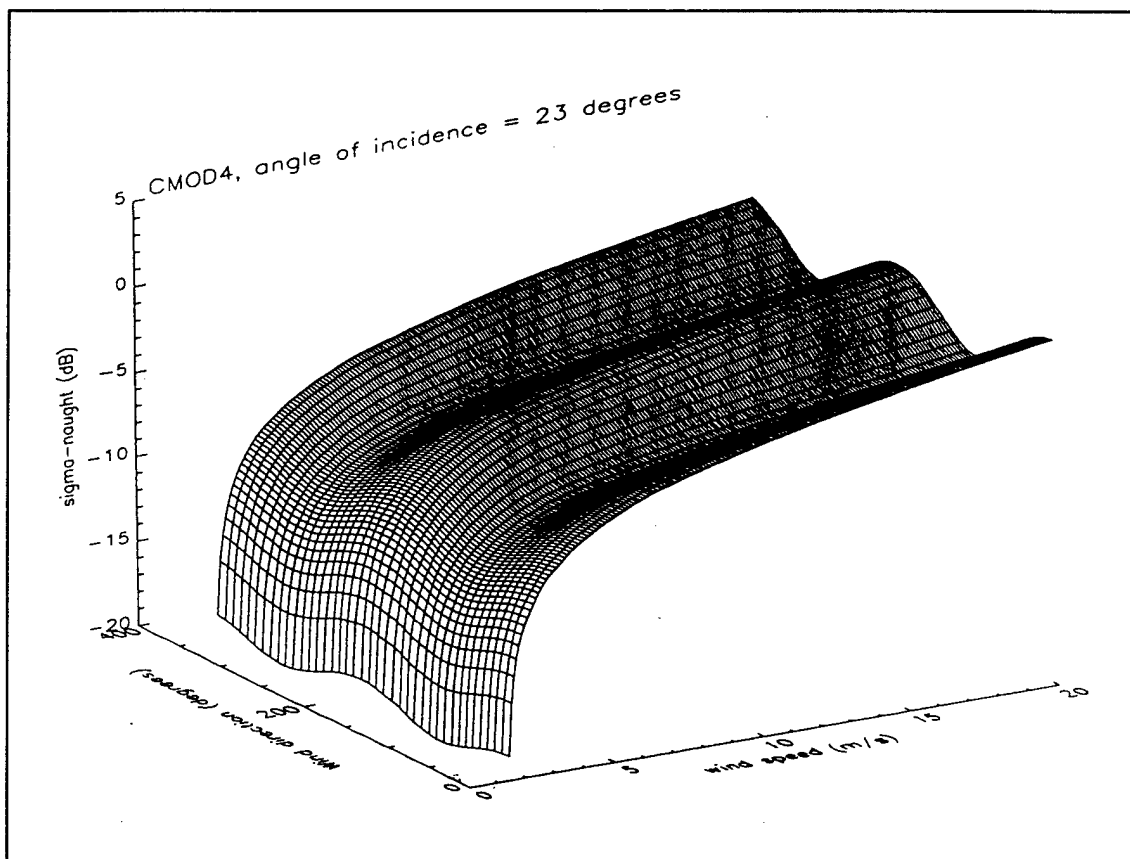


**Figure 3.5** The Radar Backscatter Dependency of Wind Directions Ranging From  $0^{\circ}$  to  $360^{\circ}$  and Wind Speeds Ranging from 2 m/s to 20 m/s at  $23^{\circ}$  Incident Angle. The Accuracy is Given to  $15^{\circ}$  in Relative Wind Direction and 2 m/s in Wind Speed

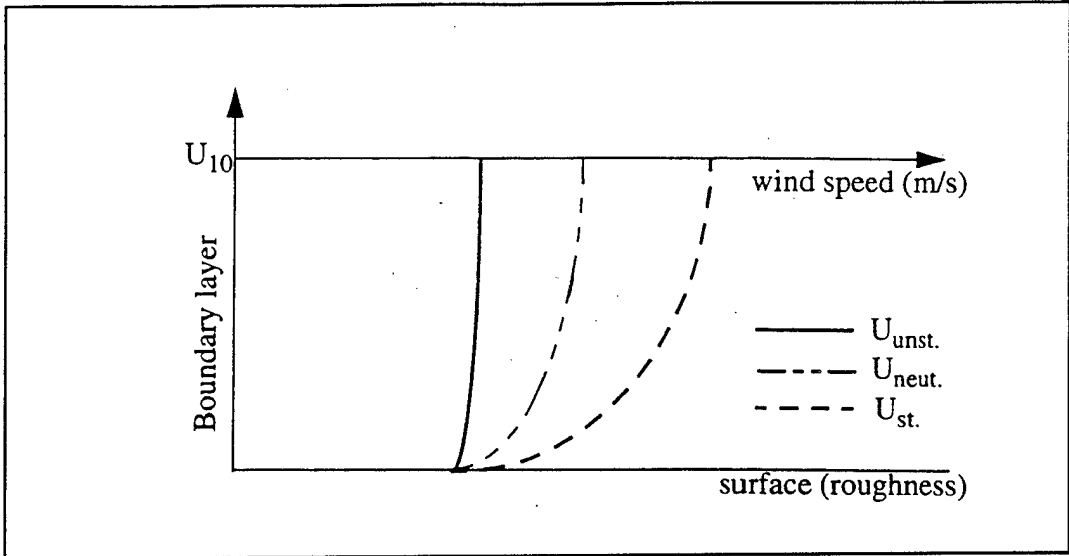


**Figure 3.6** Wind Speed at 10 m Associated with Three Different Conditions for the Stratification under the Assumption of a Constant Sea Surface Roughness.

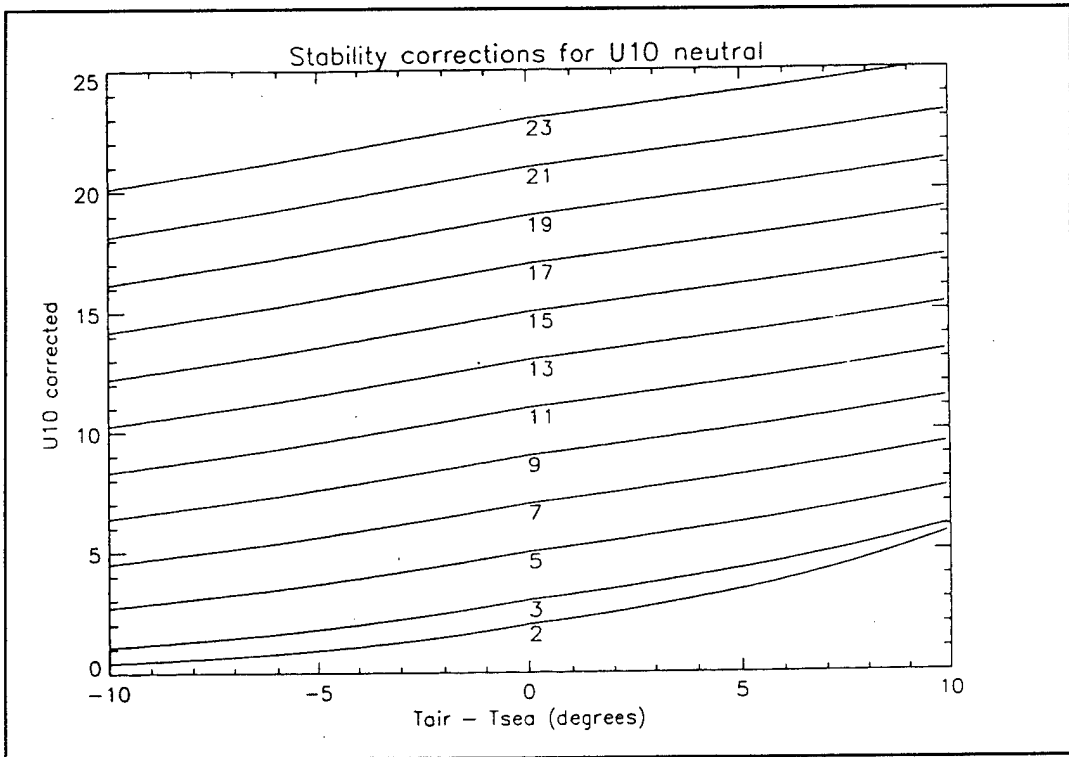


**Figure 3.7** The  $U_{10 \text{ corrected}}$  Wind Speed as a Function of  $\Delta T$  for Different  $U_{10}$  Neutral Wind Speeds (2 - 23 m/s).

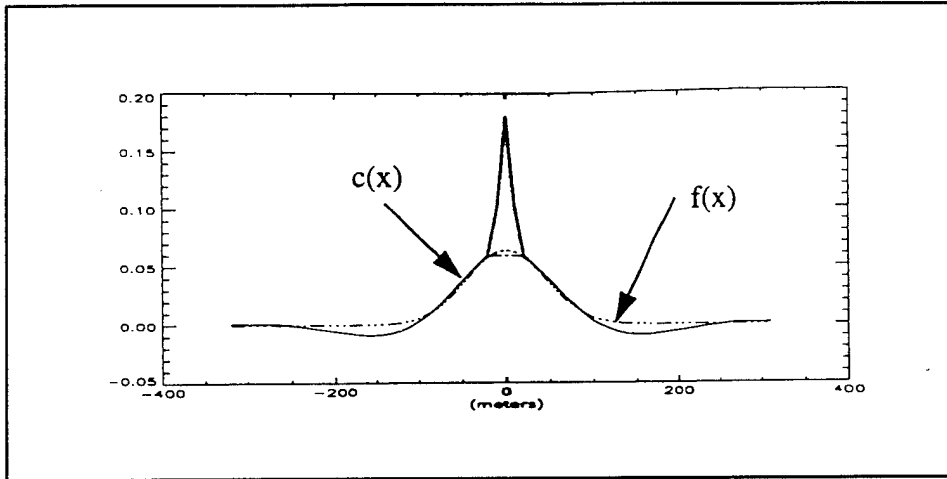


**Figure 3.8** Plot of the autocovariance function  $c(x)$  (solid line) and the fitted Gaussian function  $f(x)$  (dotted line) to the broadest part of the function, the cut-off wavelength ( $\lambda_c$ ) from this scene is estimated to be 203 m.

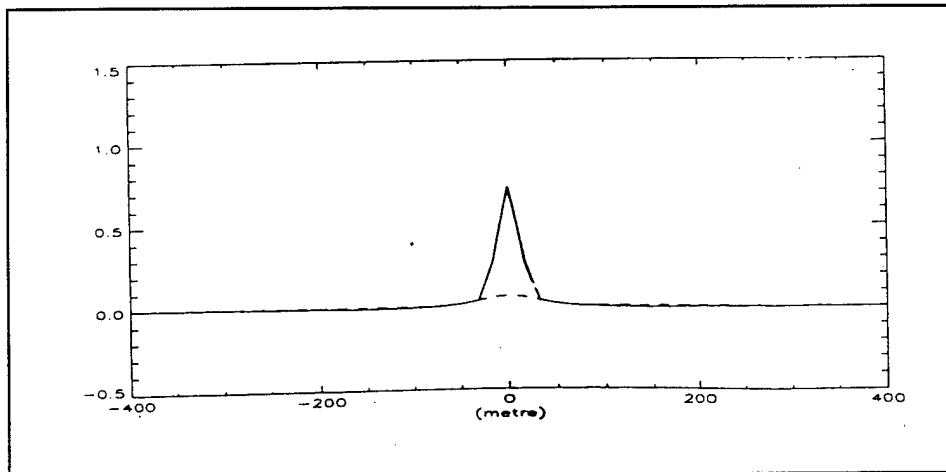


**Figure 3.9** Plot of the autocovariance function (solid line) and the fitted Gaussian function (dotted line) to the broadest part of the function, the cut-off wavelength ( $\lambda_c$ ) from this scene is estimated to be 132 m.

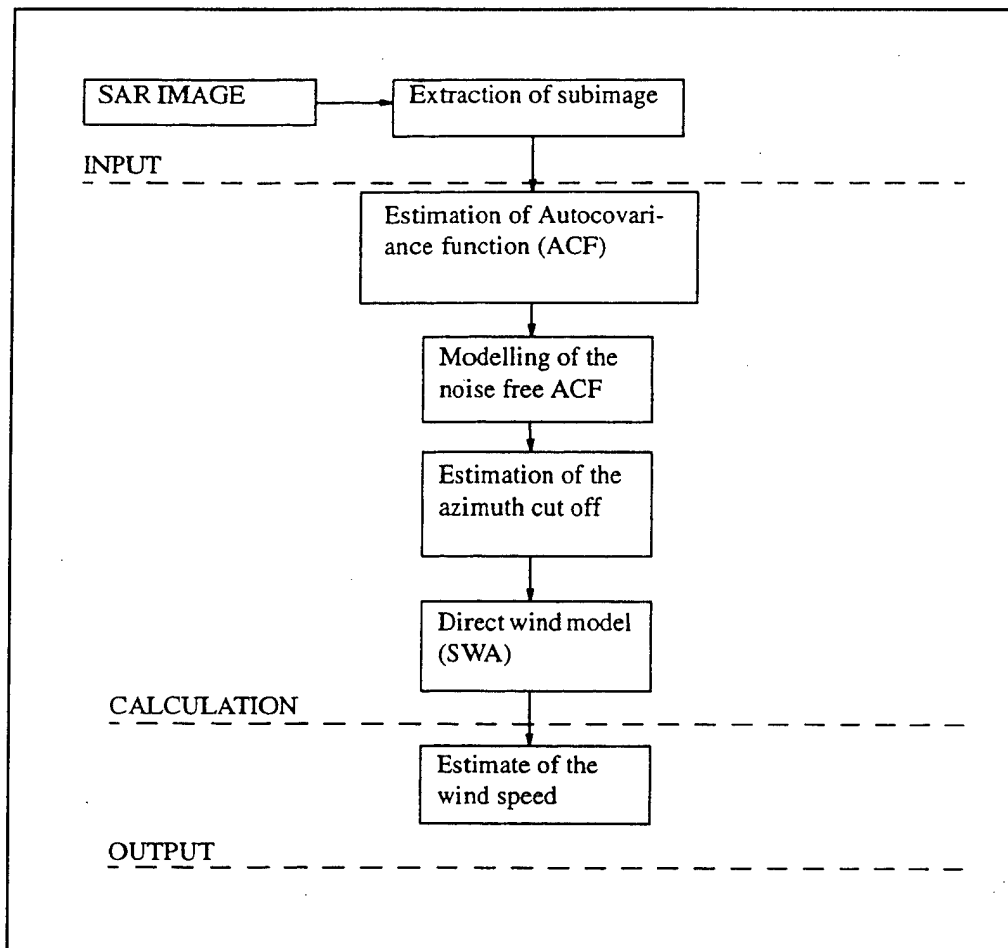


**Figure 3.10** Overview of the Calculation of the Required Parameters for the SWA

## IV. OBSERVATIONS

### A. GENERAL

During NORCSEX '95 there were very few days when both the ship and the buoy were in the SAR swath. Two of these days were 16 and 17 September and they will be examined in some detail. Unfortunately CMOD4 results are only available for the 17th, but on this day they show very good agreement with SWA. The SAR images from the 23 and 27 September overpasses show some interesting features that are related to complex coastal wind fields. Both CMOD4 and SWA results are available and are briefly reviewed for these two days.

### B. 16 AND 17 SEPTEMBER 1995

#### 1. Atmospheric Synoptic Scale

At the time of the SAR overpass on 16 September, the ship was in the vicinity of the buoy in the same SAR sub-image, at  $58^{\circ} 30' N$ ,  $4^{\circ} 46' E$  (Figure 4.1). By the time of the SAR overpass on 17 September the ship had moved about 100 km north and 50 km east of the buoy position, and was on the outside edge of the adjacent sub-image to that containing the buoy (Figure 4.2).

The 0900 Z surface analyses from 15, 16, and 17 September 1995 by the Bergen, Norway, Western Norway Meteorology Center are presented in Figures 4.3 through 4.5. The analyses show there was little change in the synoptic weather pattern during these three days in the vicinity of the NORCSEX '95 experiment. At the beginning of this period there was a high pressure center to the northeast of Norway and a double low to the southeast with centers over the English Channel and the North Sea. The North Sea low extended north along the southwest

coast of Norway to form an inverted trough over the NORCSEX area. A warm front extended eastward from the North Sea low associated with overcast and precipitation over southern Norway and northern Denmark. On the 16th ridging from the Norway high had partially filled in the North Sea low and the western portion of the warm front had moved north to parallel the southeast coast of Norway through the NORCSEX area while the eastern portion of the front remained almost stationary over northern Denmark. By the morning of the 17th the North Sea low had completely filled and the warm front was oriented east to west again over Denmark.

The scale of these surface charts illustrates what is normally available to the user and are an excellent example of why a mesoscale wind field would be of value. In the absence of the plotted observations, the surface wind would be expected to circulate counter-clockwise around the low pressure centers and clockwise around the high pressure centers. The direction would run roughly  $15^\circ$  cross isobar toward the lower pressure. Wind speed is proportional to the gradient of the isobars. Given only this information one would infer that the wind direction in the vicinity of the NPS buoy on at 0900 on 15 September was generally from the southeast and it gradually shifted to the south southeast and decreased in magnitude by 0900 on 16 September. The direction then appears to stay fairly constant through 17 September with some additional decrease in magnitude. Looking closely at the observations in the area of the NPS buoy it can be seen that many of the wind vectors cross the isobars at nearly  $90^\circ$  and there is a great deal more mesoscale variation than the scale of the chart or the density of the observations can show.

## **2. Atmospheric Mesoscale**

The radiosonde profiles (Figures 4.6 and 4.7) are from the R/V *Hakon Mosby* as near as possible to the time of the SAR overpasses. The radiosondes measured information from the

ascending and descending soundings producing double traces. It is obvious that the atmosphere on both days was quite similar. The profiles show southeast surface winds that agree fairly well in both magnitude and direction with the surface analysis (Figures 4.4 and 4.5), potential temperature increasing slowly with height, and specific humidity decreasing with height. Both days show a well mixed boundary layer with a slightly unstable air-sea temperature difference.

Figures 4.8 and 4.9 present a time series of ten minute averaged meteorological variables measured on the R/V *Hakon Mosby* and the NPS buoy. The time series cover seventy-two hours from 0000 on 15 September to 0000 on 18 September and show the wind speed (adjusted to 10 m), true wind direction, air and sea temperatures, friction velocity ( $u^*$ ) computed using bulk methods, and the surface pressure. Examination of this time series shows good agreement with the surface weather maps (Figures 4.3 through 4.5). The sea level pressure slowly increased from 15 through 17 September as the anticyclone passed by to the North and the inverted trough over the North Sea weakened. During this time the wind gradually shifted from east to southeast. At the buoy, wind speed increased from approximately 6 m/s at 0500 on the 15th to 16 m/s at about 0520 on the 16th and then steadily decreased to about 8 m/s by 2200 on the 16th when it remained fairly constant through the SAR overpass on the 17th.

There is very good agreement between the propeller anemometer and the sonic anemometer mounted on the R/V *Hakon Mosby* over the entire period, and between the ship and buoy measurements while they were side by side.

### **3. CMOD4 and SWA Results vs. In-situ Data**

#### ***a. Wind Algorithm Model Results***

The SAR images used for the analysis are roughly 100 by 100 km. These are

divided into sub-images for processing which are roughly 10 by 10 km. The scale of the sub-images is dependent on computer memory and processing time. For CMOD4 processing, the pixels in the sub-image are averaged to 100 by 100 m resolution, an estimated wind direction is entered, and the output is averaged to yield one wind vector for each sub-image. For the SWA model, the SAR image power spectrum is calculated from each sub-image and the SWA model then returns one wind speed for each sub-image. The SAR images used on 16 and 17 September are shown in figures 4.10 through 4.15. These are descending scenes with north at the top of the page. Image number one is the farthest north. The nine by nine matrix shows the sub-images described above. For both 16 and 17 September the images show increasing backscatter (lighter pixels) to the south as the wind speed increases, and northwest to southeast oriented wind streaks (more evident on 16 September) which are in general agreement with the in-situ wind direction.

The Chapter III discussion of the CMOD4 and SWA wind models showed that, although they are both related to the radar backscatter, they are significantly different. The SWA model is dependent on the azimuth cutoff wavelength which is a function of the SAR integration time and the wind speed, while the CMOD4 model is directly related to the radar backscatter from the Bragg scattering waves. While the models can be used independently, it may be more useful combine them in some way. Although not complete, Korsbakken's (1996) examination of SAR data from NORCSEX '95 shows very good agreement between CMOD4 and SWA computed wind speeds assuming a 2 m/s accuracy in each of the models. He has developed an algorithm for an optimum wind vector using the SWA and CMOD4 models illustrated in Figure 4.16.

The optimum wind vectors obtained using Korsbakken's algorithm for 17 September are shown in Figure 4.17. The 'holes' in the coverage are where the difference between model wind



speeds exceeded 2 m/s. The wind vectors shown outside of the SAR swath are from the Norwegian Meteorological Services HINDCAST model for 10 m winds. Table 2 presents a summary of the results of the SWA, CMOD4 and in-situ wind speeds for 16 September in the sub-image containing the NPS buoy and the R/V *Hakon Mosby*, and for 17 September in the adjacent sub-images containing the NPS buoy and the R/V *Hakon Mosby*. Table 2 also compares wind values between the ship and both models for 27 September, to be discussed later.

<b>Table 2: Comparison of modeled and in-situ wind speed</b>			
	SWA	CMOD4	In-situ
16 Sep 1995	9 m/s	Not available	11 m/s (buoy) 11 m/s (ship)
17 Sep 1995	10 m/s 4 m/s	10 m/s 4 m/s	11 m/s (buoy) 6 m/s (ship)
27 Sep 1995	11 m/s	5 m/s	9 m/s (ship)

On the 16th, SWA results are somewhat lower than the in-situ measurements but fall within the assumed 2 m/s accuracy window of the in-situ wind. At the time of the SAR overpass on 17 September, CMOD4, SWA, and in-situ all agree within 2 m/s. Since there is no in-situ data in the areas where CMOD4 and SWA differed by more than 2 m/s (Figure 4.17) it is difficult to say why such difference occurred. There were very few sub-images which had a difference in modeled wind speeds of greater than 4 m/s.

### C. 23 SEPTEMBER 1995

Figures 4.18 and 4.19 are the SAR images from 23 September. They are from a descending path with image number one the farthest to the north. Both images are shown with

north toward the top of the page. Figure 4.18 shows the Norwegian coast running roughly from the upper right to the lower left corner of the image. Just off the coast there appears to be some orographically sheltered areas with less backscatter with wind speed increasing to the southeast. The most dominant feature on this day is the large curved frontal feature evident in the center left area of image number two (Figure 4.19). From analysis of the two model wind fields this appears to be a small wind front on the order of 2 m/s. The R/V *Hakon Mosby* was north of this feature at the time of the overpass. However, the ship turned south along a track that would intersect it at approximately 90°. If the front remained stationary the ship should have crossed it at about 1800. A meteorological time series (Figure 4.20) from the ship shows a fairly steady backing of the wind and a general decrease in wind speed until almost 2000 when the wind begins to increase steadily. It is possible that this is the frontal feature observed in the SAR image. However, this connection has to be viewed with caution due to the variability in the wind speed and the elapsed time since the overpass. The scale of this wind front is on the order of 10 km and clearly does not show up on the synoptic weather map shown in Figure 4.21. It is just discernable in the combined wind vector plot in Figure 4.22.

#### **D. 27 SEPTEMBER 1995**

The SAR images for 27 September, (Figure 4.23 and 4.24) are from a descending path again with north toward the top of the page. Figure 4.26 is a preliminary map pointing out some of the features such as wind streaks, SST fronts, internal waves, temperature fronts, and rain showers visible in the images (Korsbakken 1996). The R/V *Hakon Mosby* followed a triangular path in the northern image for the majority of the day crossing three SST fronts. At the time of the Satellite overpass, the in-situ wind speed was 9.2 m/s while SWA and CMOD4 winds were

10.8 and 4.8 m/s respectively. As shown in the combined wind vector plot (Figure 4.26), the two models were within 2 m/s agreement for less than 50% of the sub-images for this overpass. For the location of the R/V *Hakon Mosby*, SWA was the more accurate model and within 2 m/s of the in-situ measurement. The reasons for the model differences on this day have yet to be determined but are being investigated by the collaborative group of NORCSEX '95.

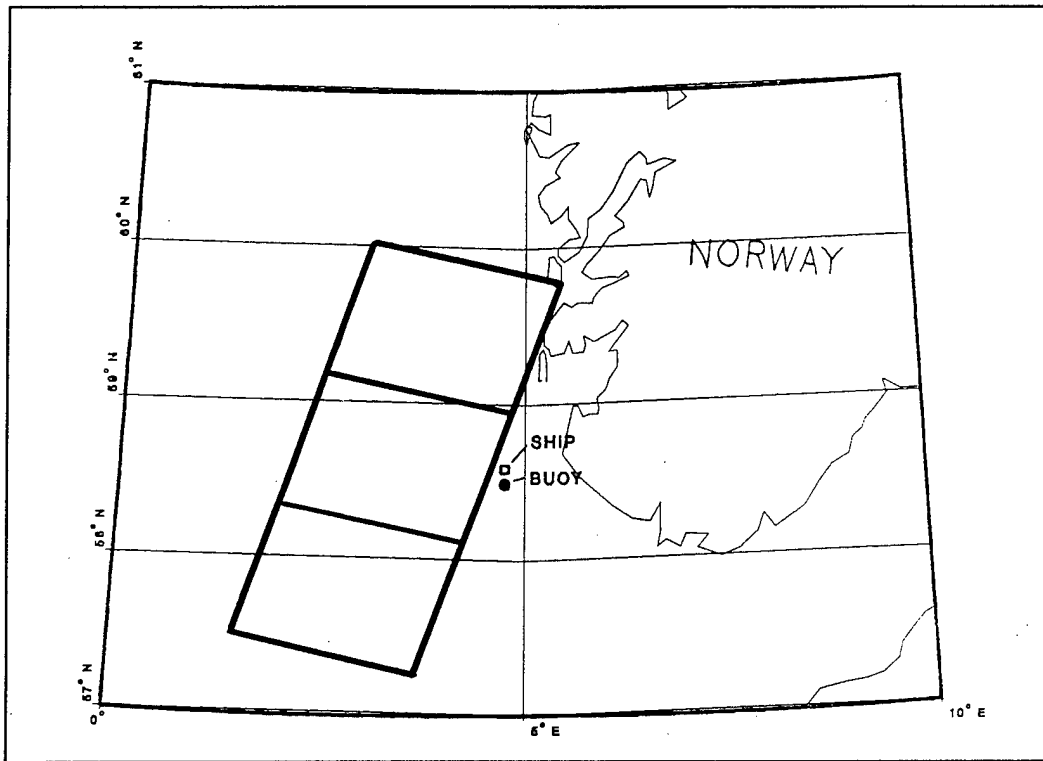
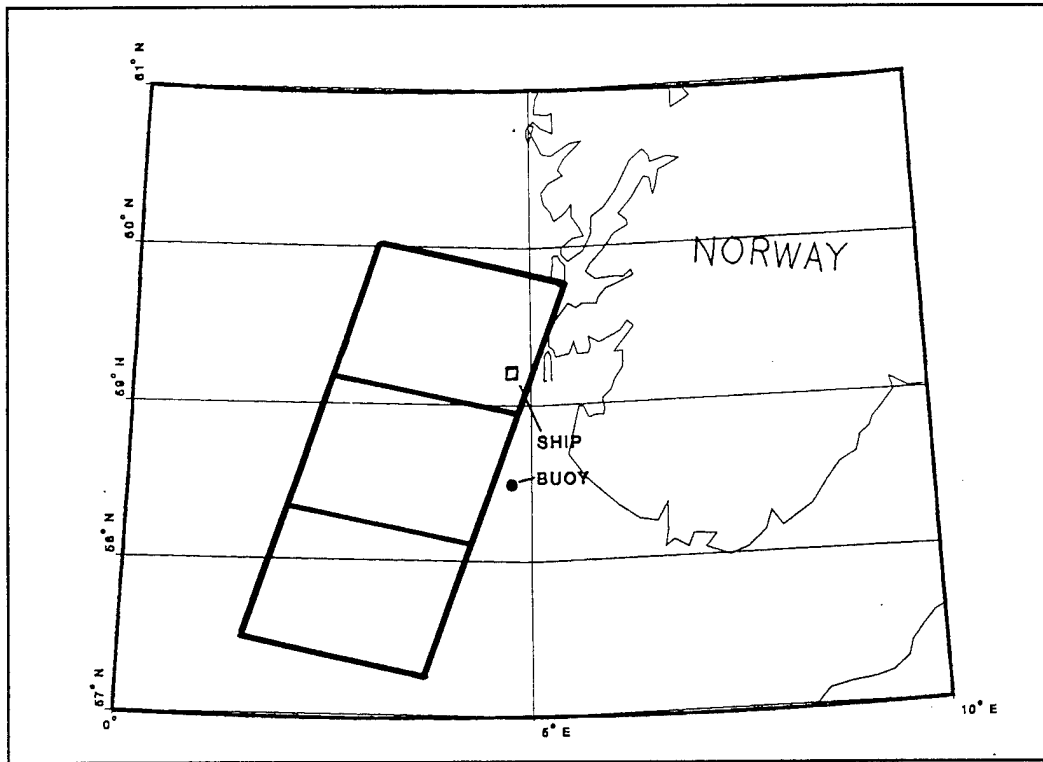


Figure 4.1 SAR Images with NPS Buoy Position and R/V *Hakon Mosby* Track for 16 September 1995.



**Figure 4.2** SAR Images with NPS Buoy Position and R/V *Hakon Mosby* Track for 17 September 1995.

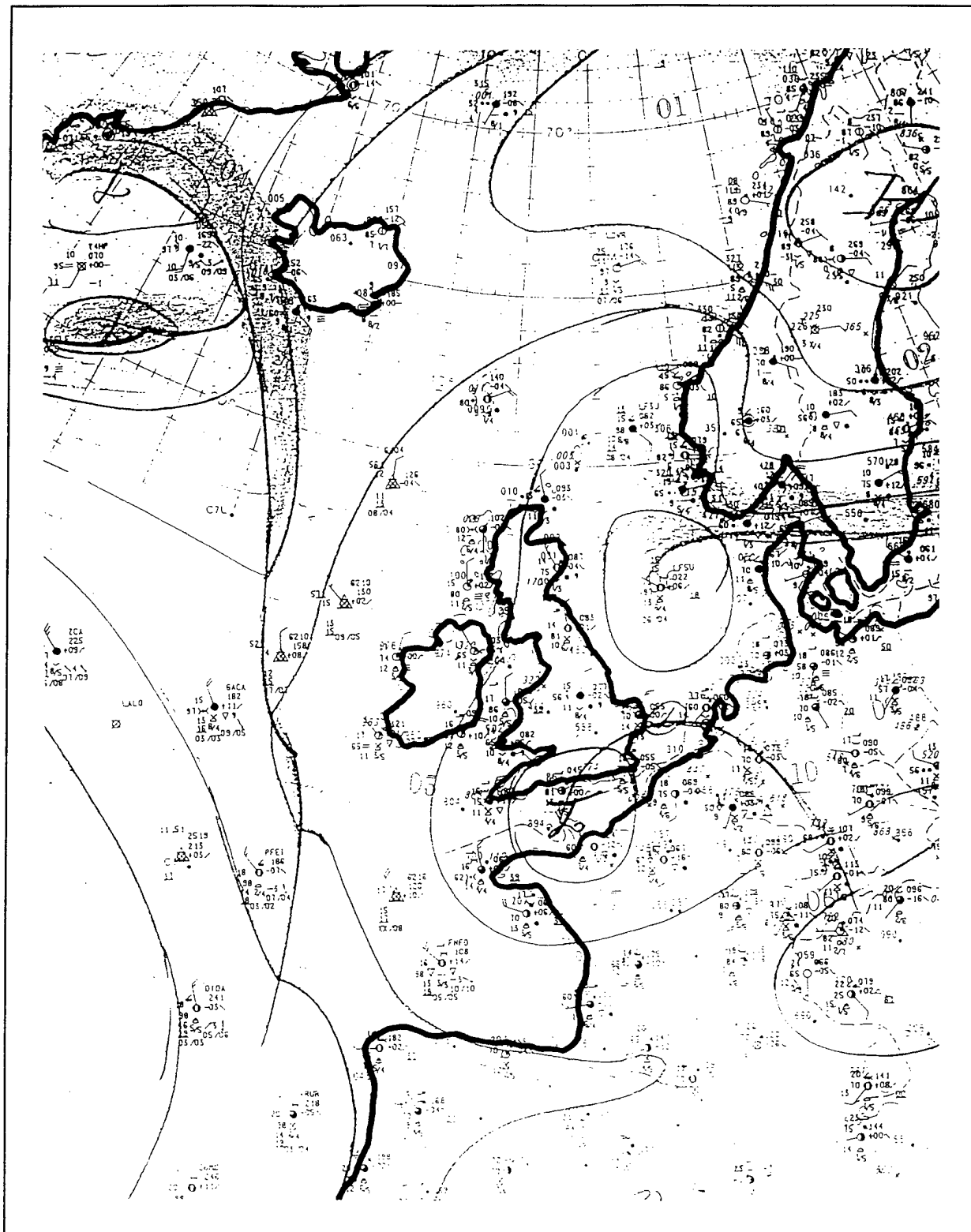


Figure 4.3 Surface Analysis for 0900 UTC 15 September 1995 Prepared by the Bergen, Norway, Western Norway Meteorology Center.

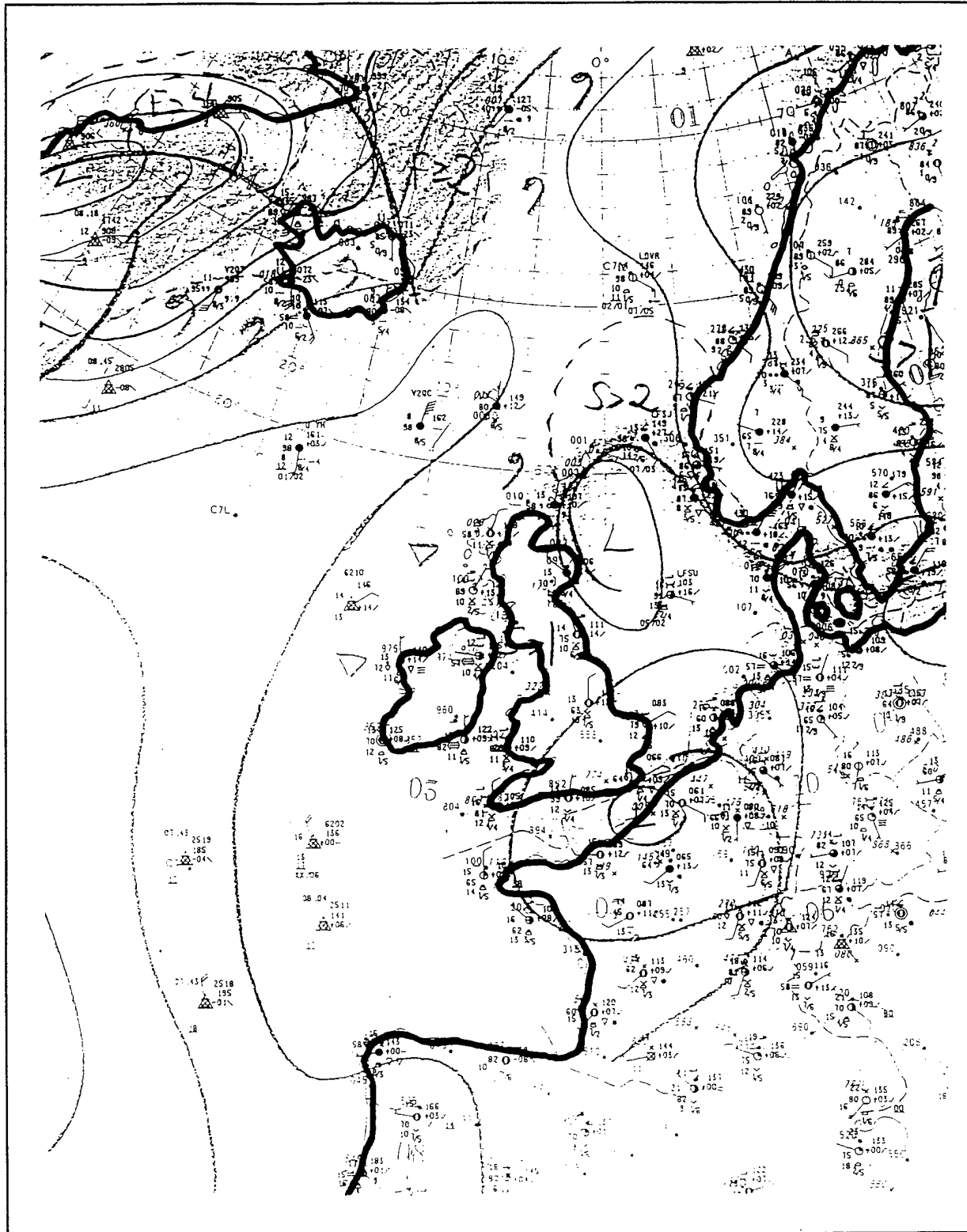


Figure 4.4 Surface Analysis for 0900 UTC 16 September 1995 Prepared by the Bergen, Norway, Western Norway Meteorology Weather.

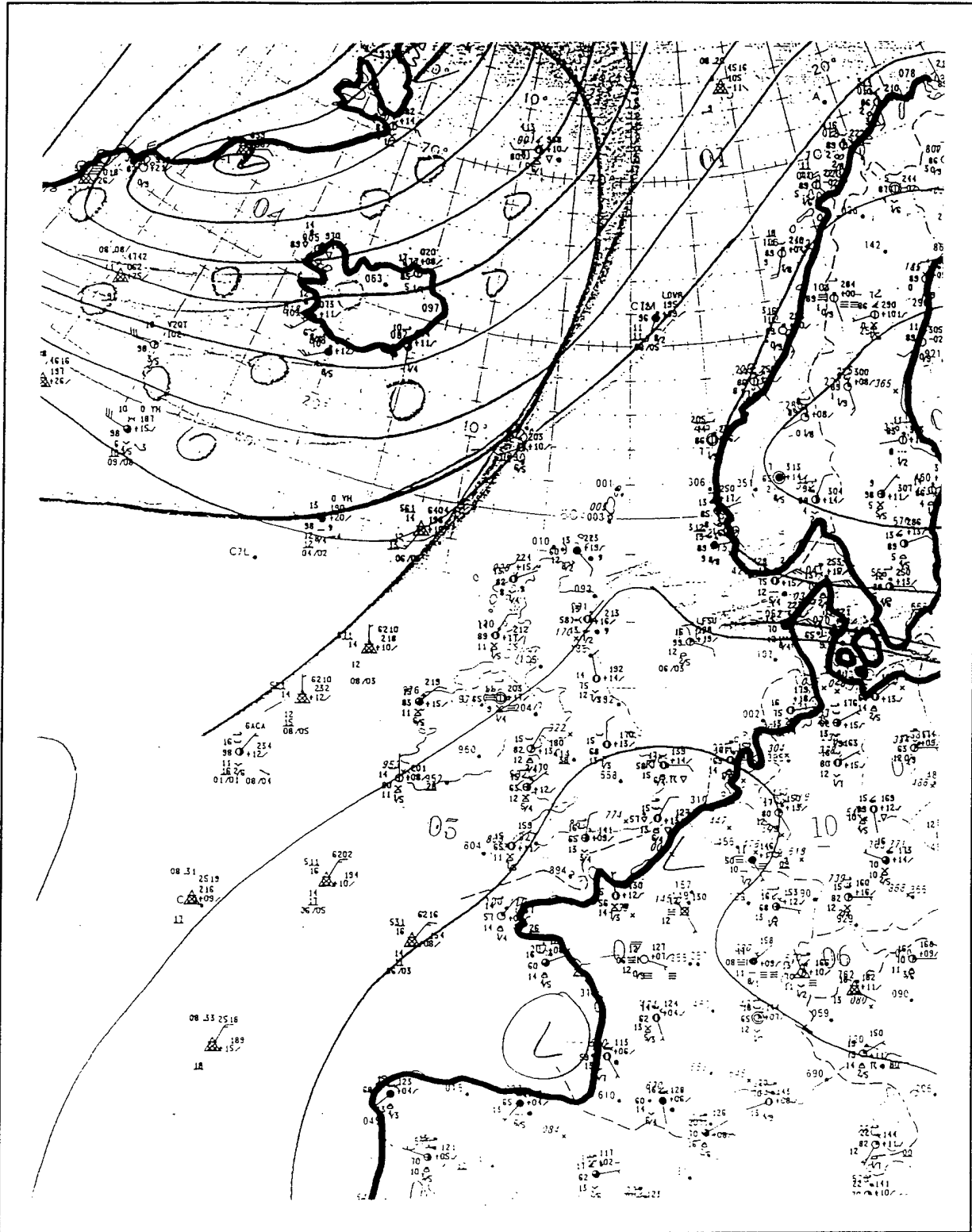


Figure 4.5 Surface Analysis for 0900 UTC 17 September 1995 Prepared by the Bergen, Norway, Western Norway Meteorology Center.



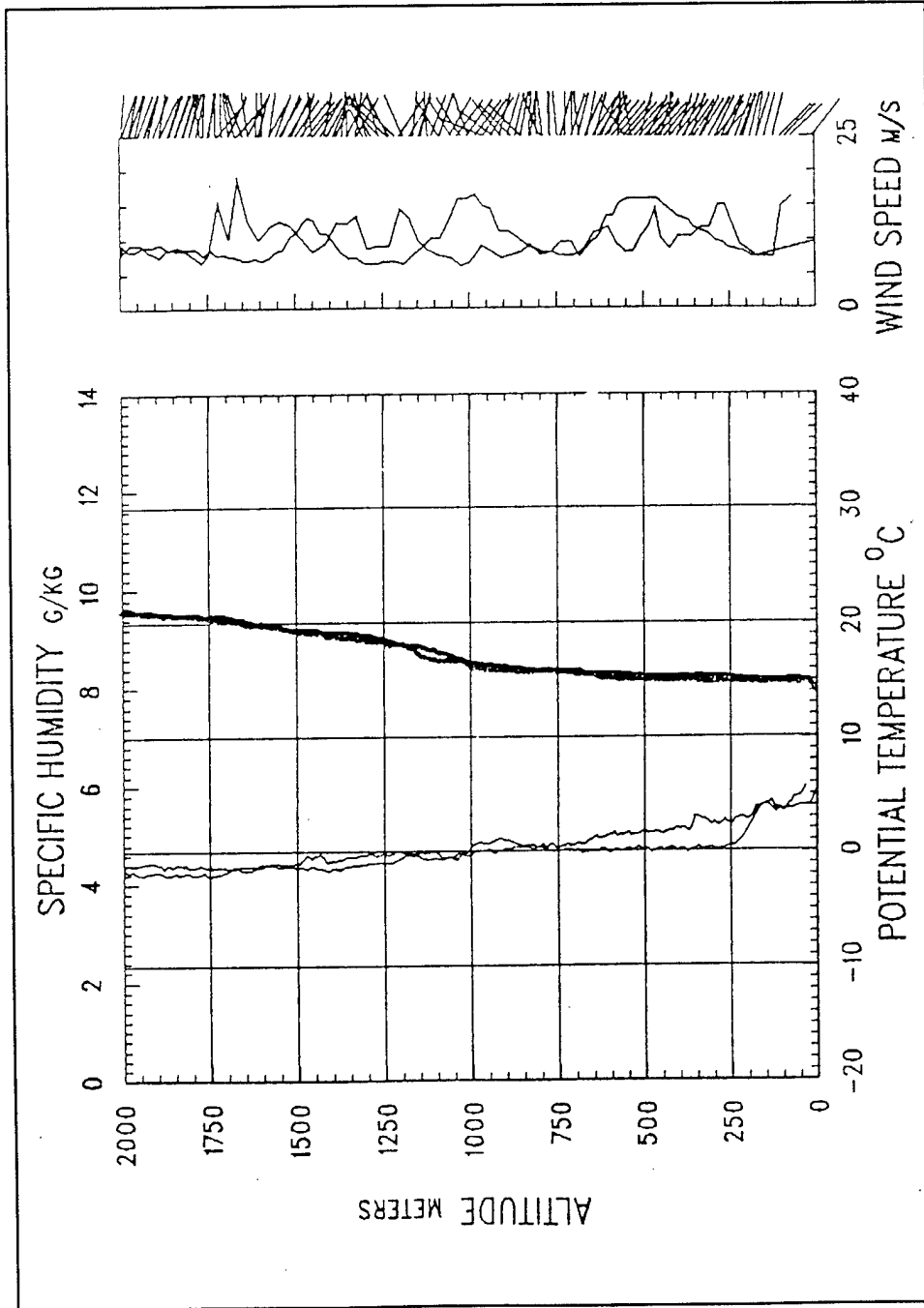


Figure 4.6 Radiosonde Profile from R/V *Hakon Mosby* 1423 UTC 16 September 1995

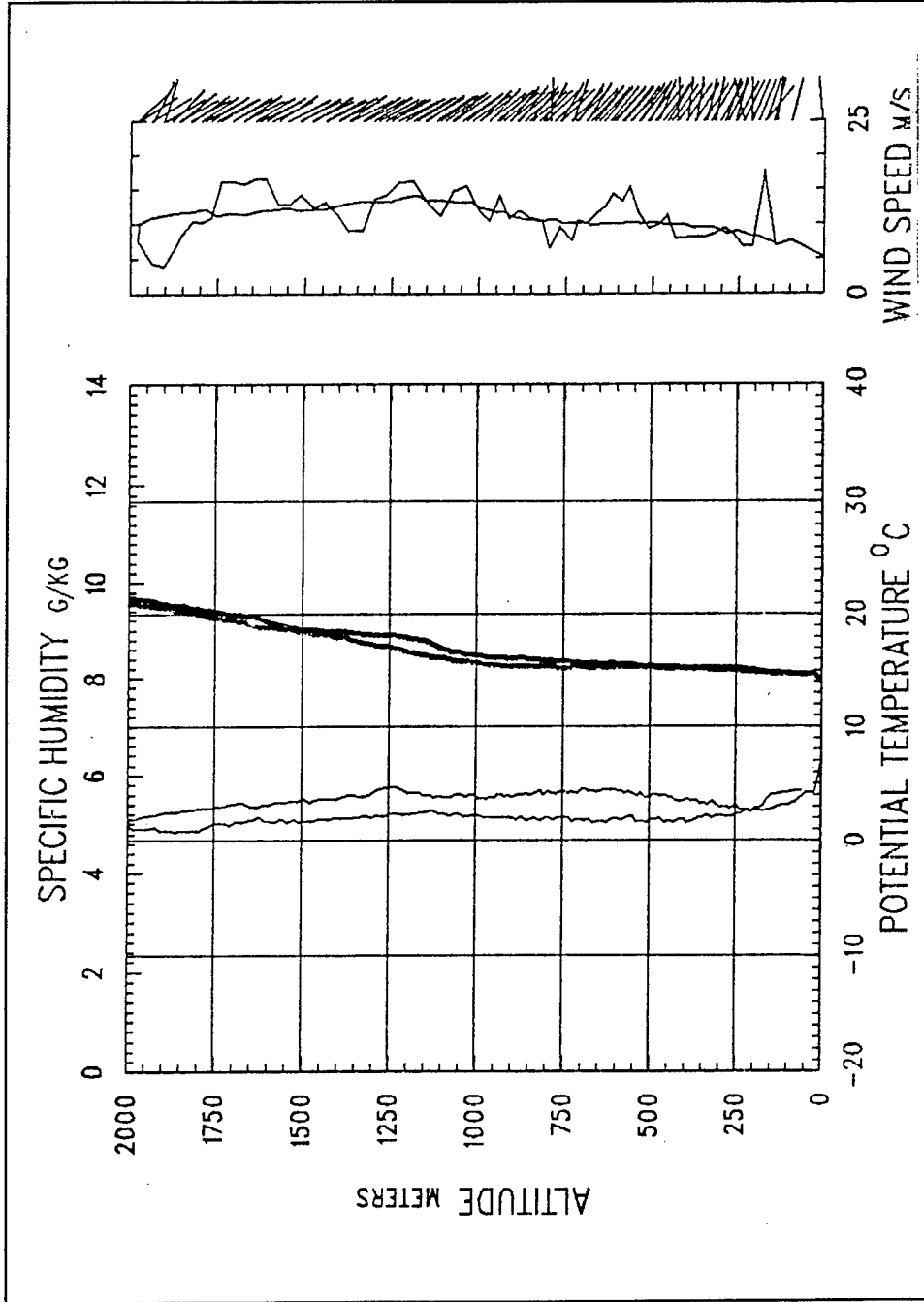
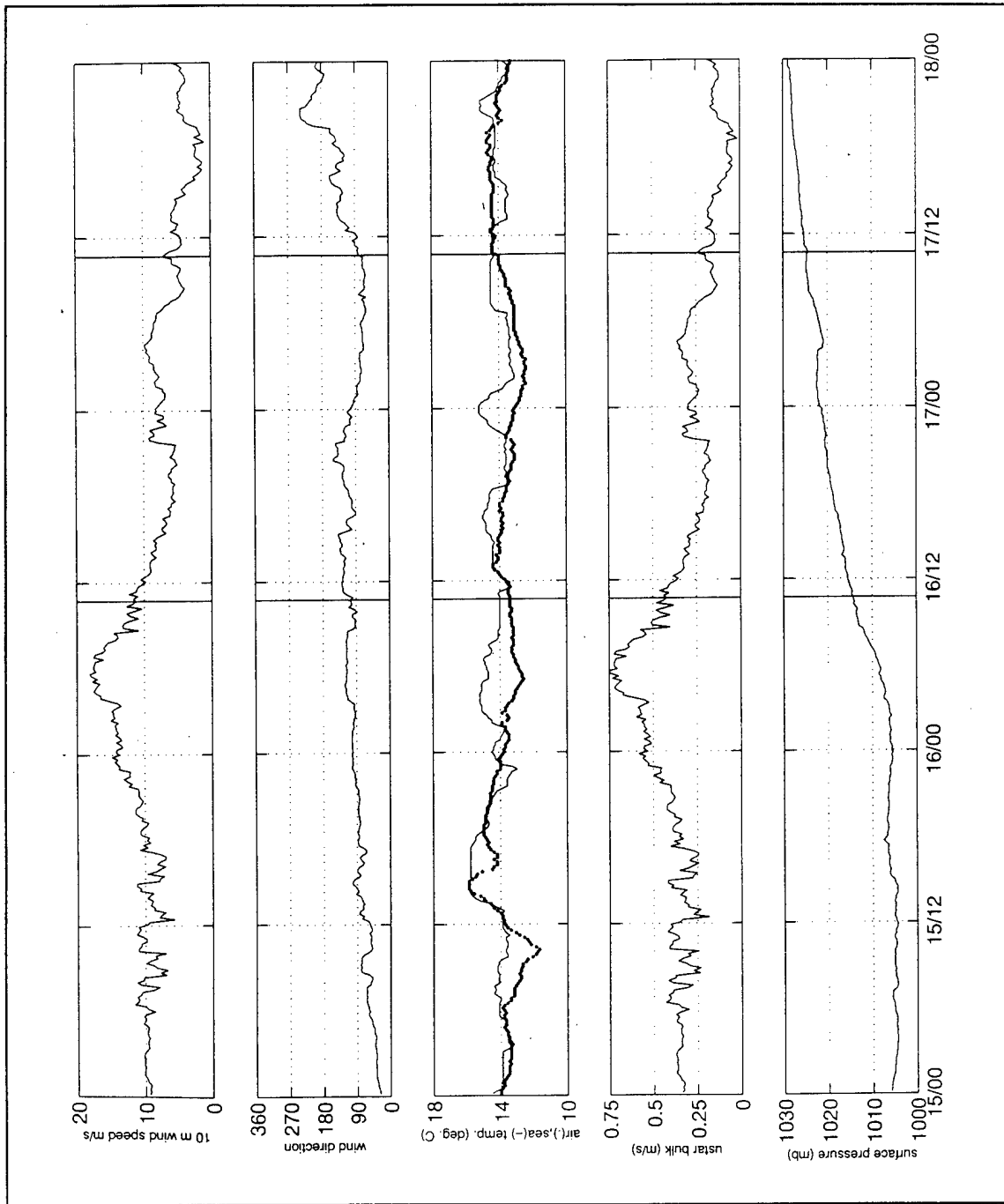
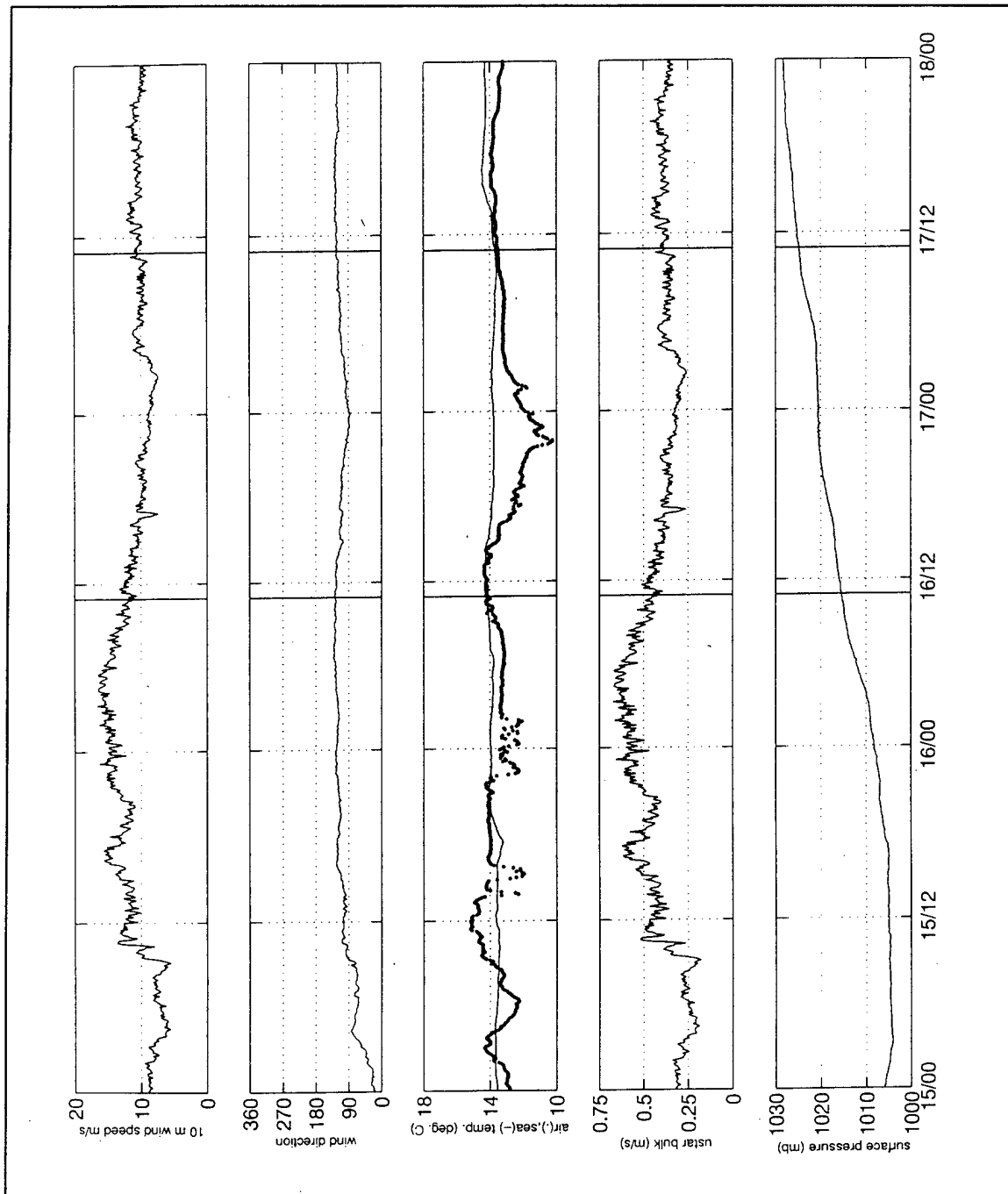


Figure 4.7 Radiosonde Profile from R/V *Hakon Mosby* 1019 UTC 17 September 1995



**Figure 4.8** Time Series of Meteorological Variables Measured on the R/V *Hakon Mosby* from 15 through 17 September 1995



**Figure 4.9** Time Series of Meteorological Variables Measured on the NPS Buoy from 15 through 17 September 1995

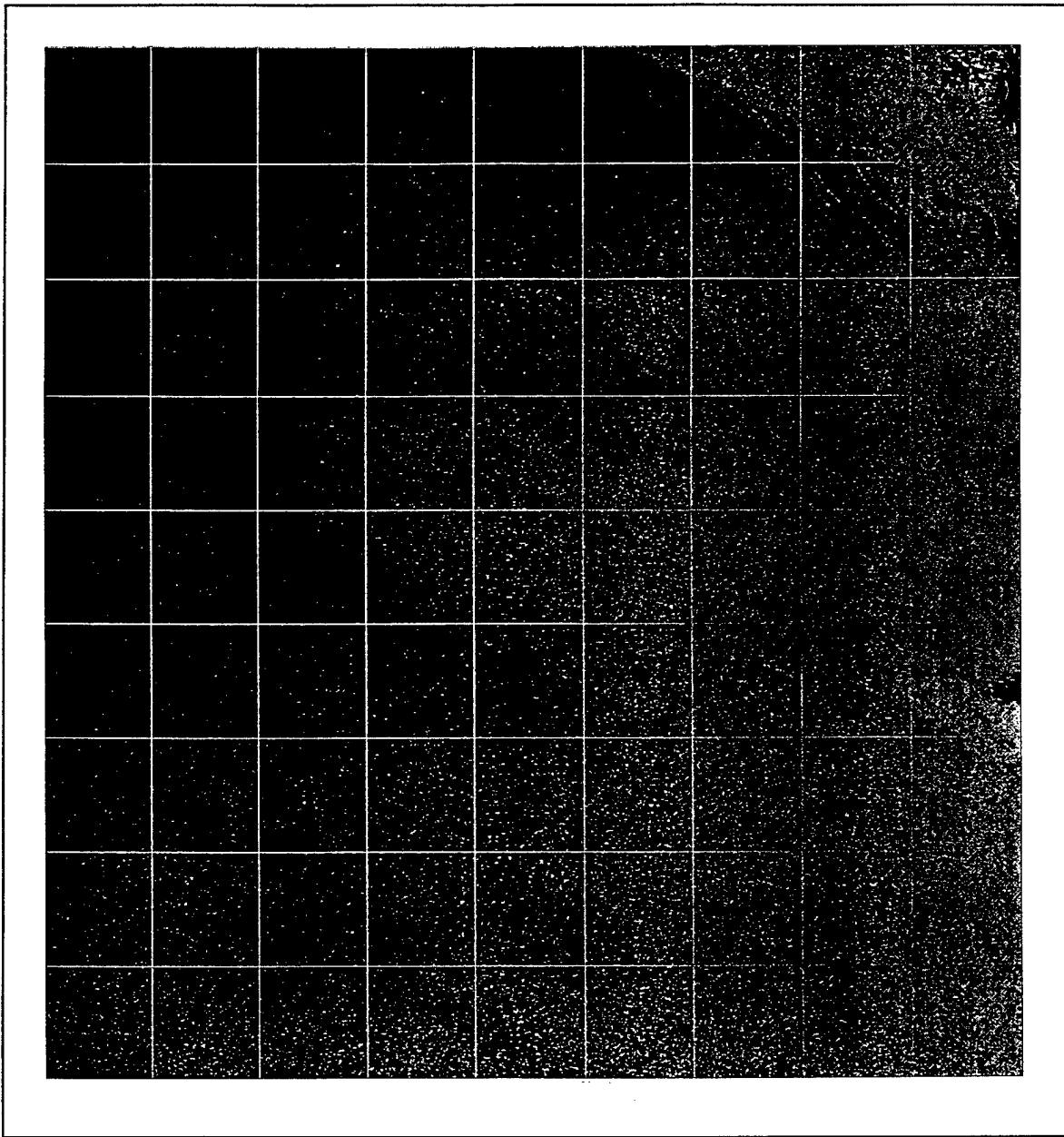


Figure 4.10 SAR Image Number One for 16 September 1995.

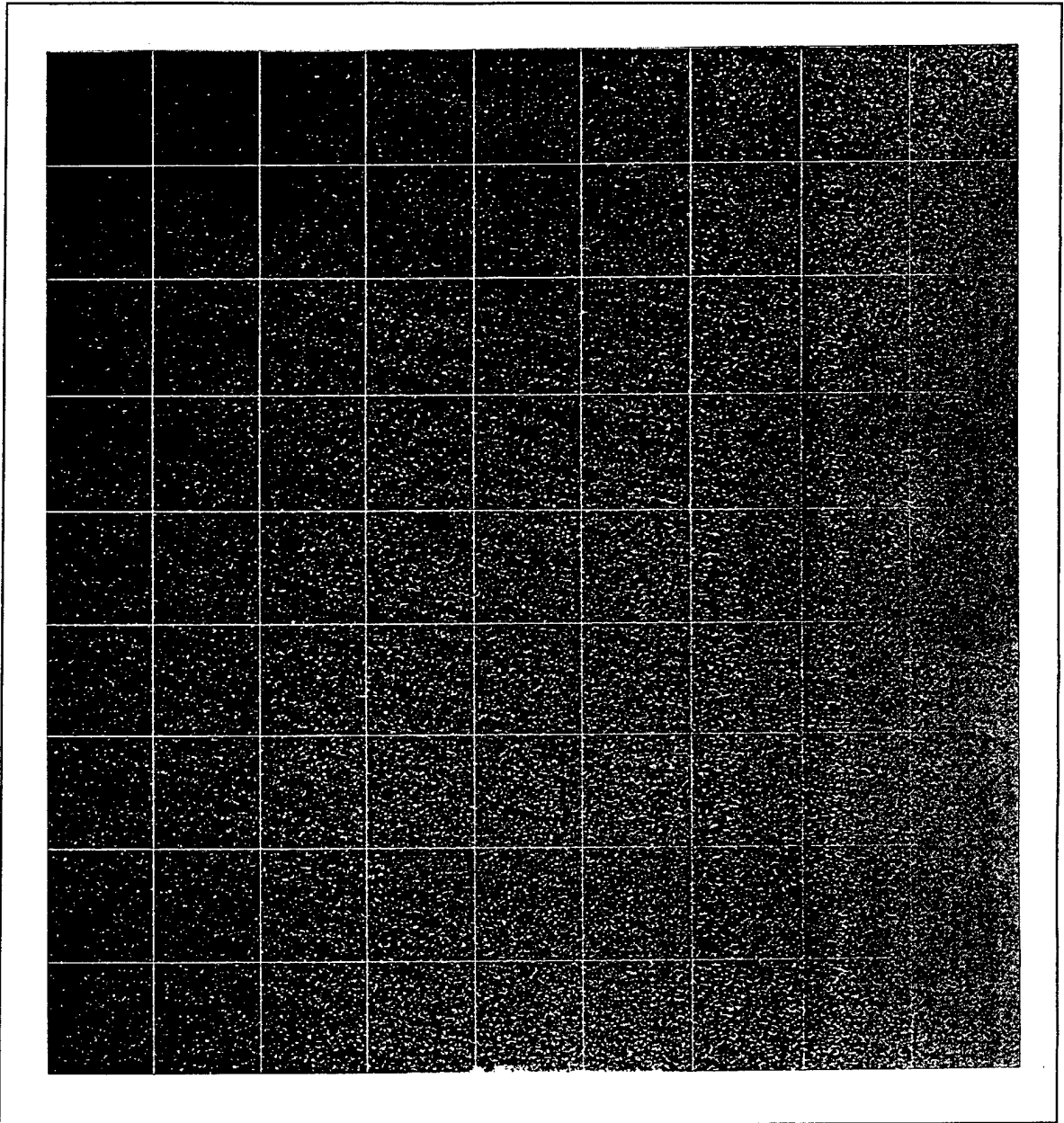


Figure 4.11 SAR Image Number Two for 16 September 1995.

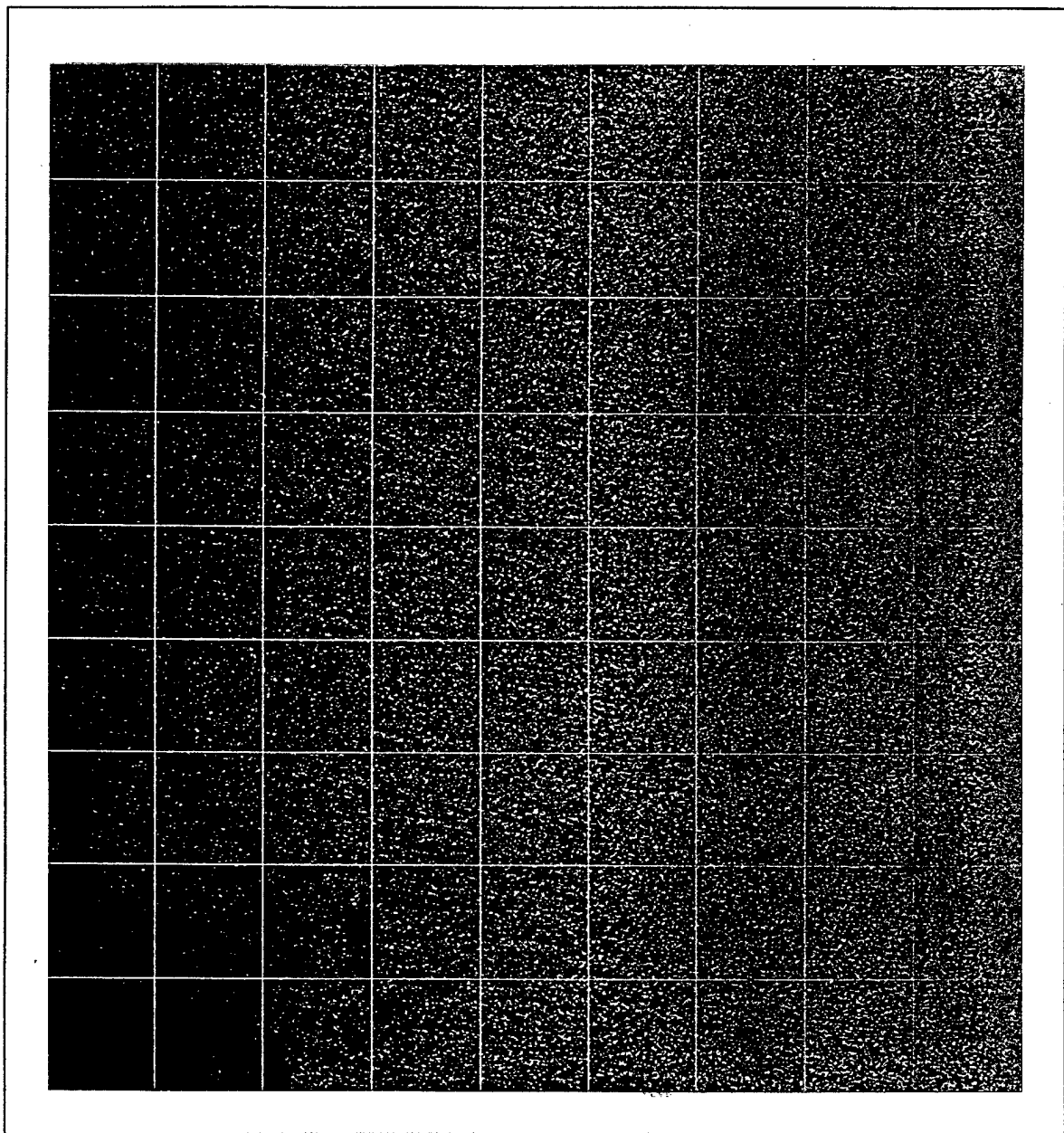


Figure 4.12 SAR Image Number Three for 16 September 1995.

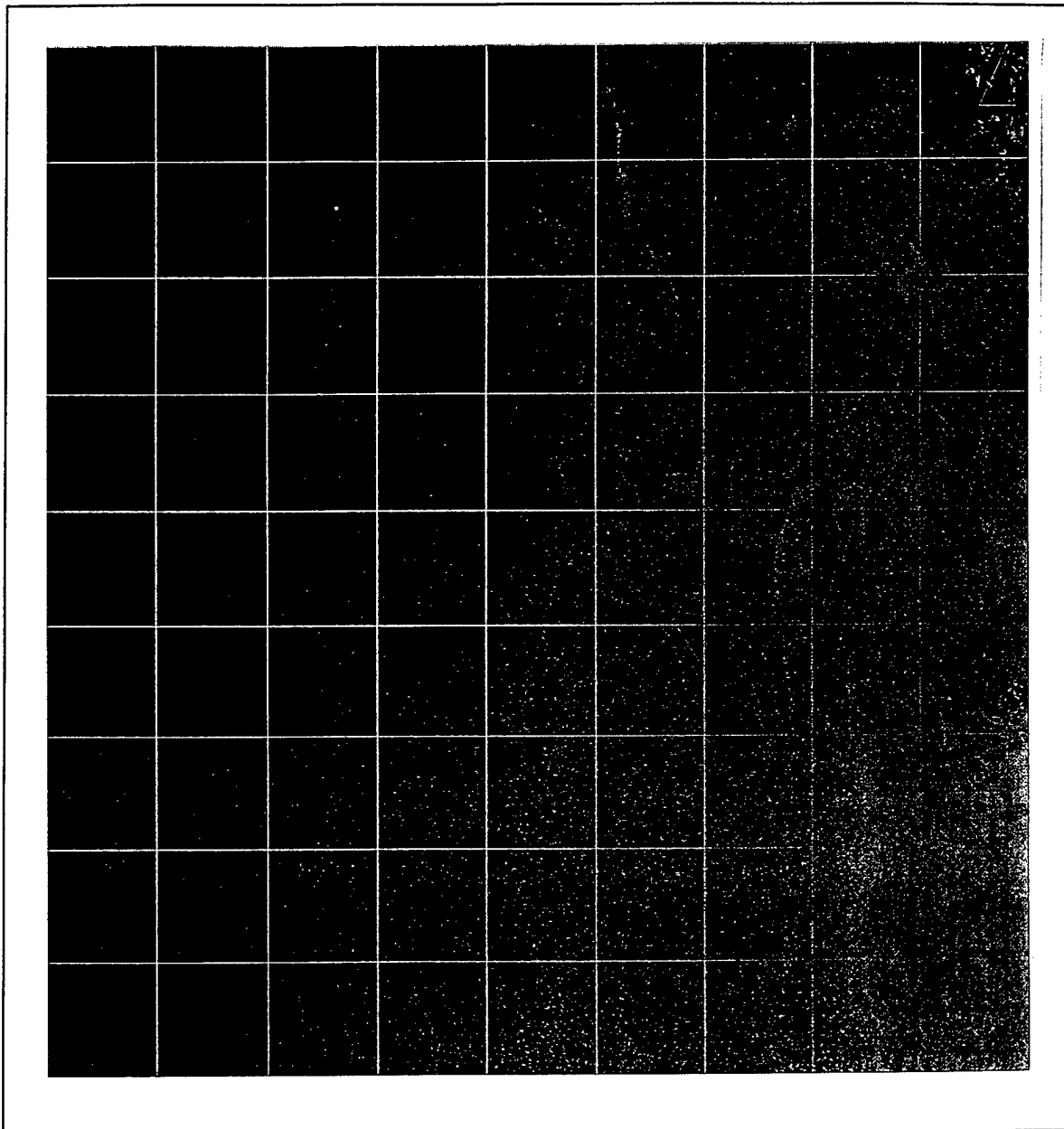


Figure 4.13 SAR Image Number One for 17 September 1995.



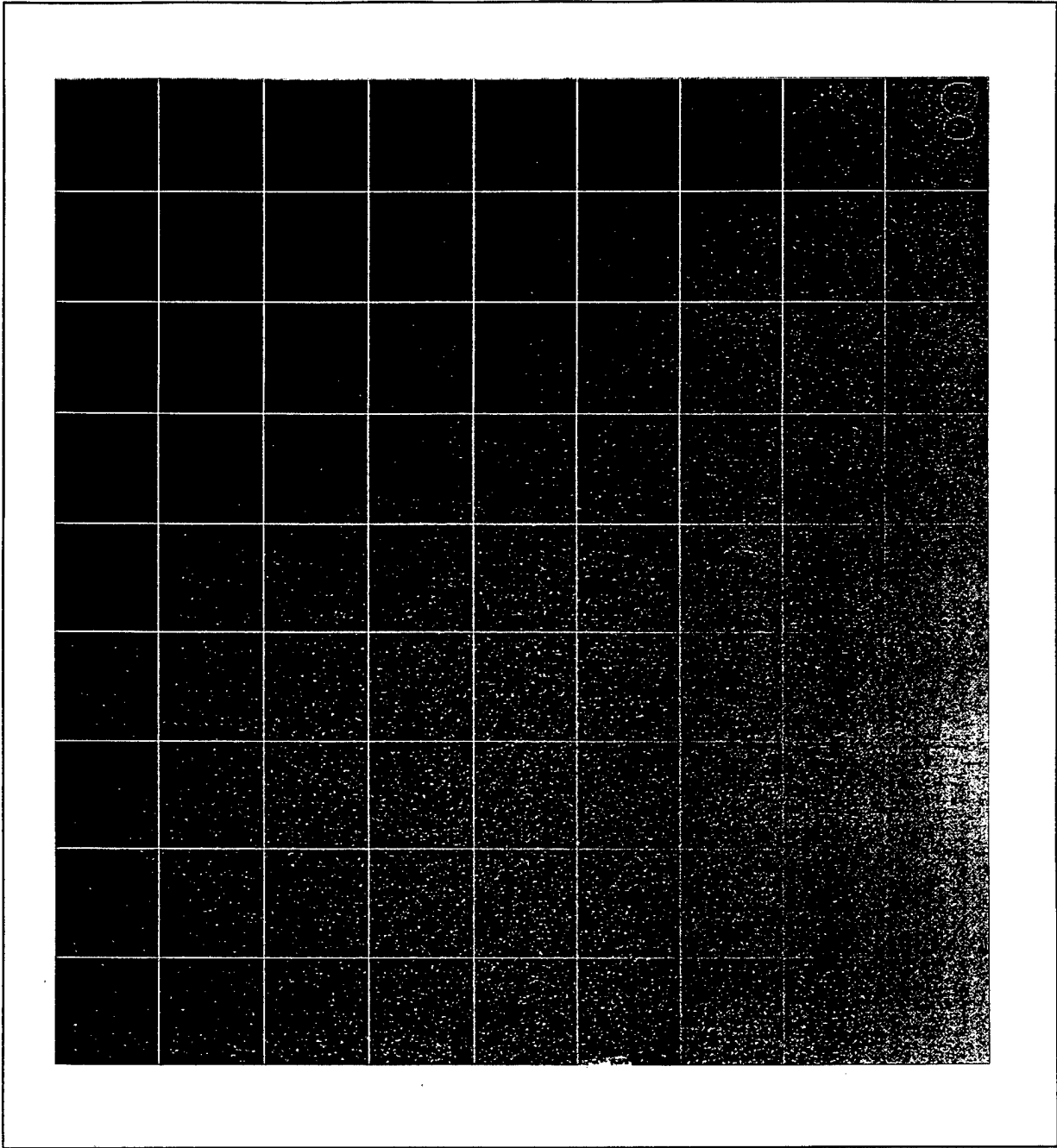
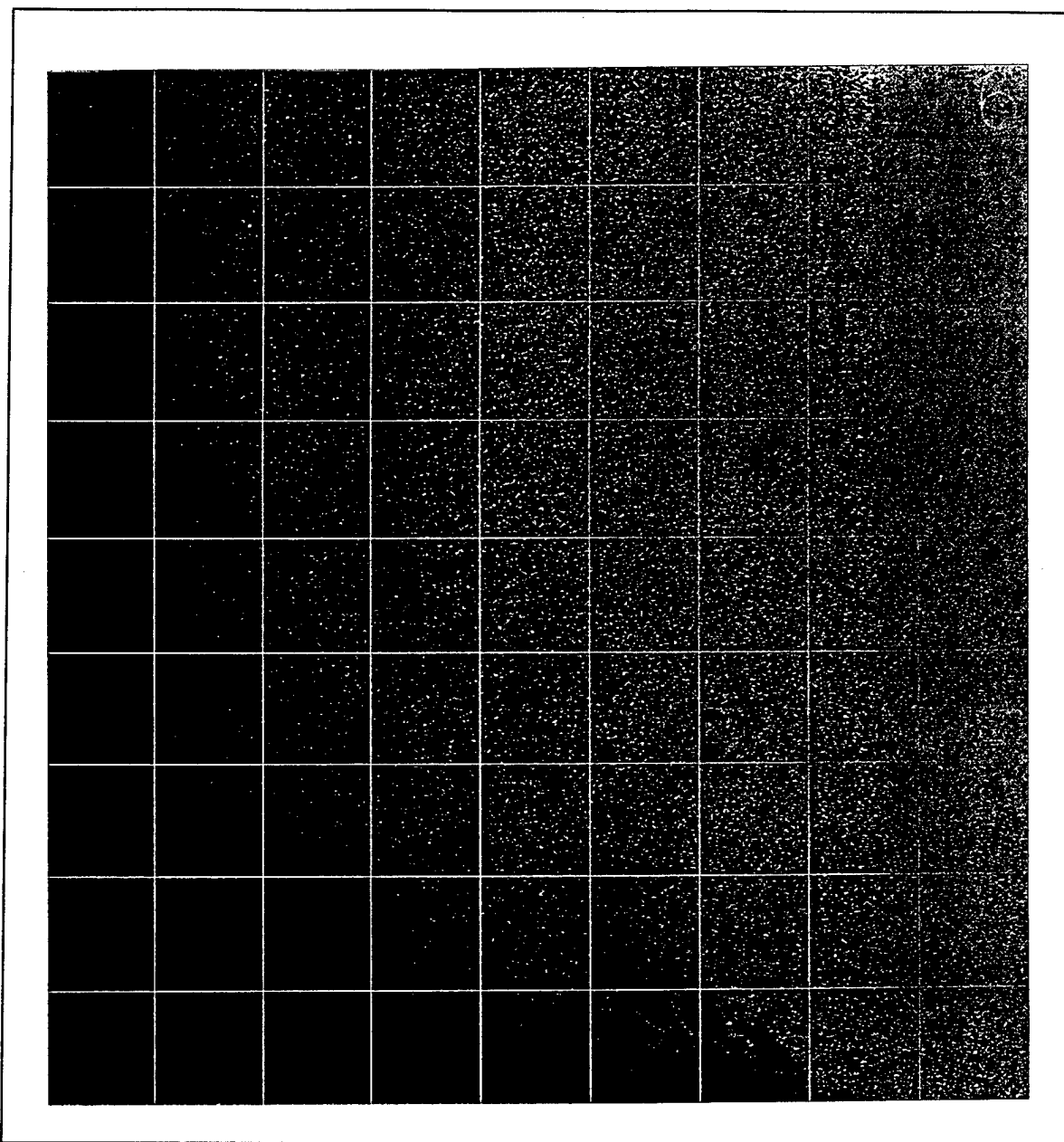


Figure 4.14 SAR Image Number Two for 17 September 1995.



**Figure 4.15** SAR Image Number Three for 17 September 1995.

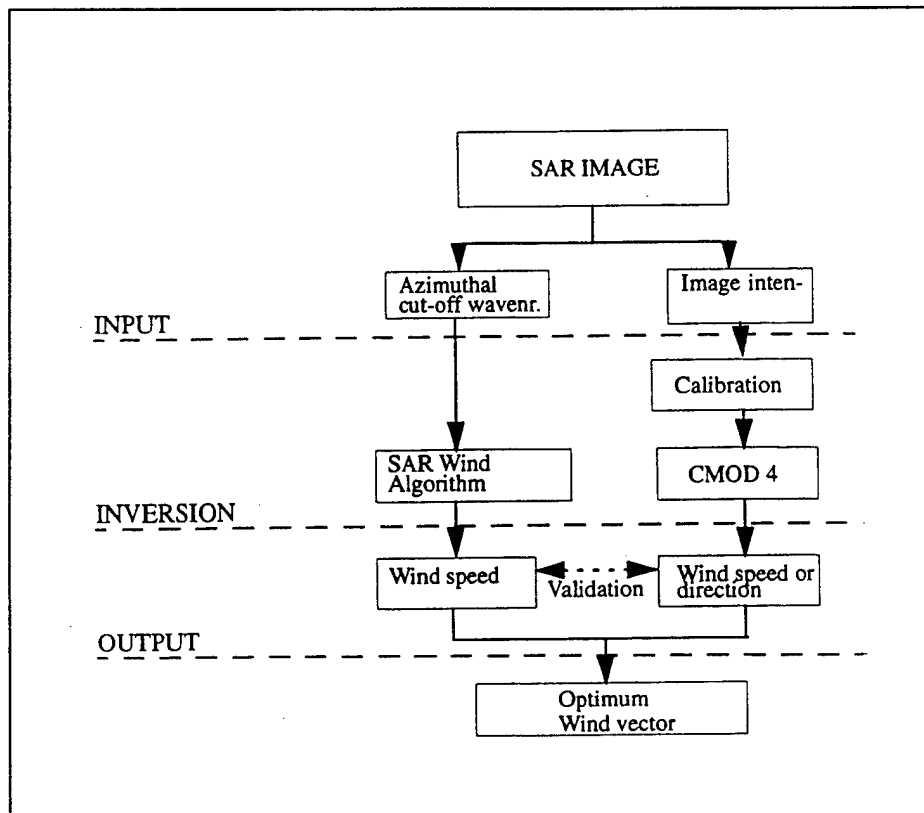


Figure 4.16 Optimum Wind Vector Algorithm for CMOD4 and SWA.

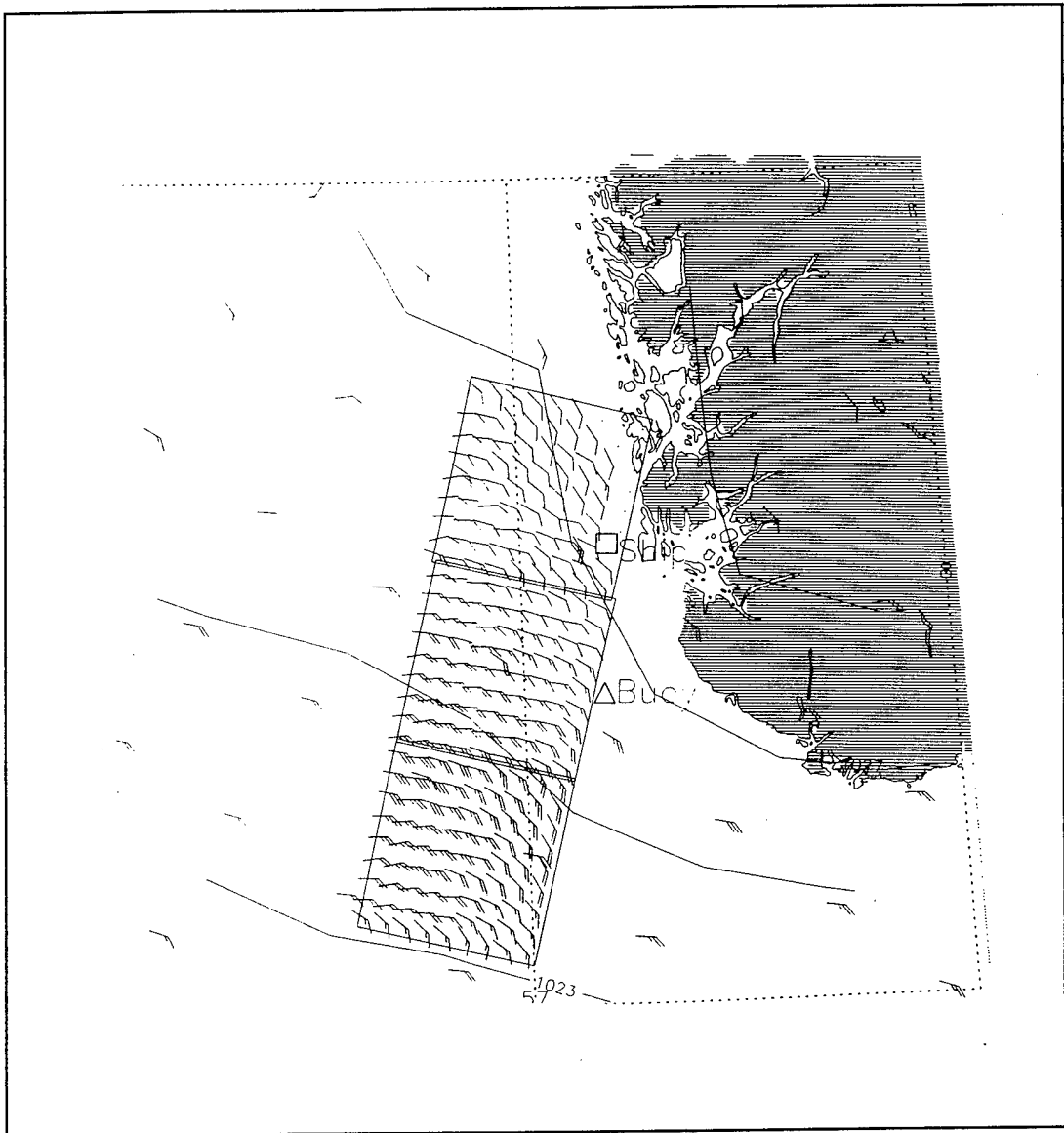


Figure 4.17 Combined Wind Vector Plot for 17 September 1995

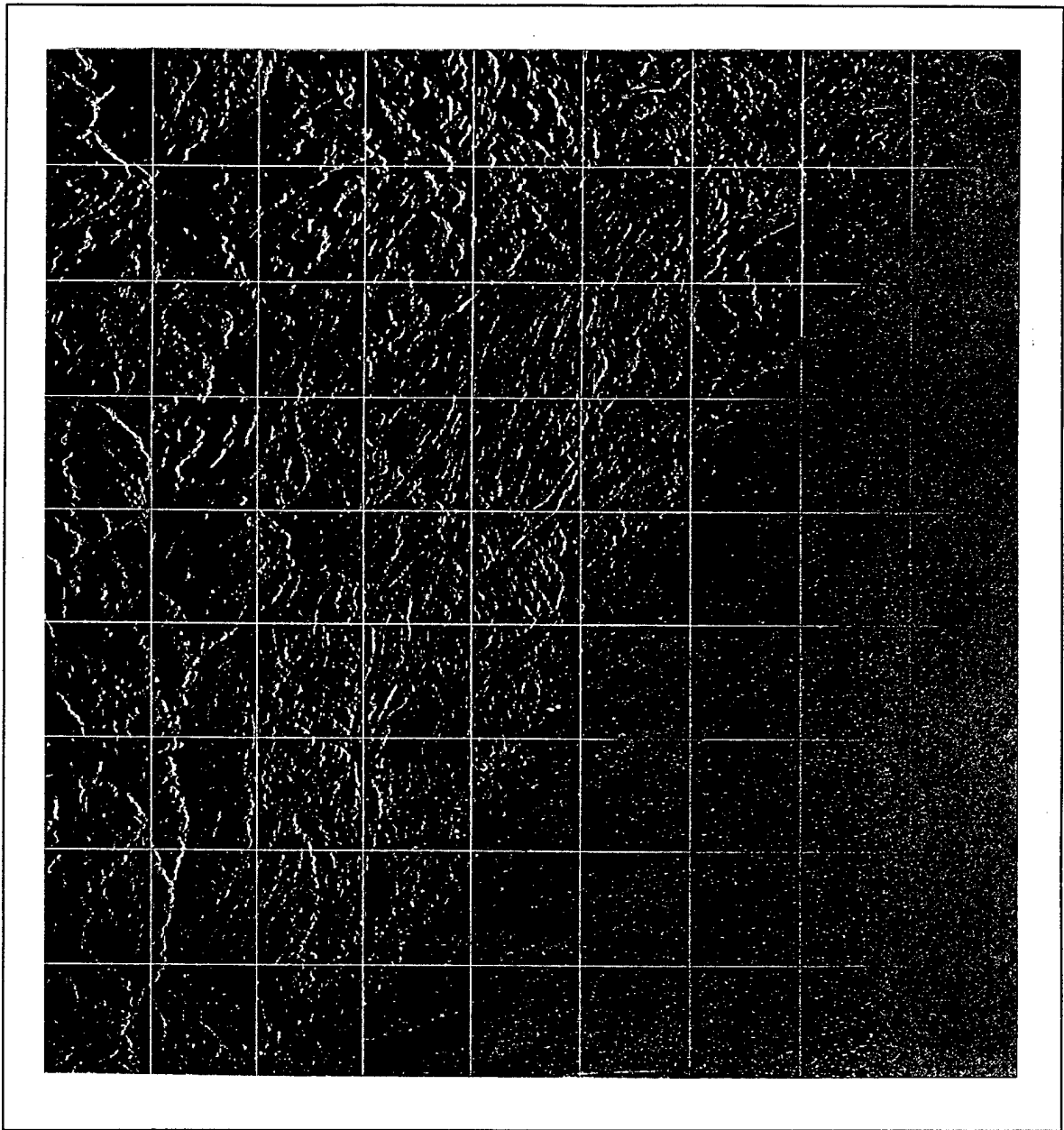
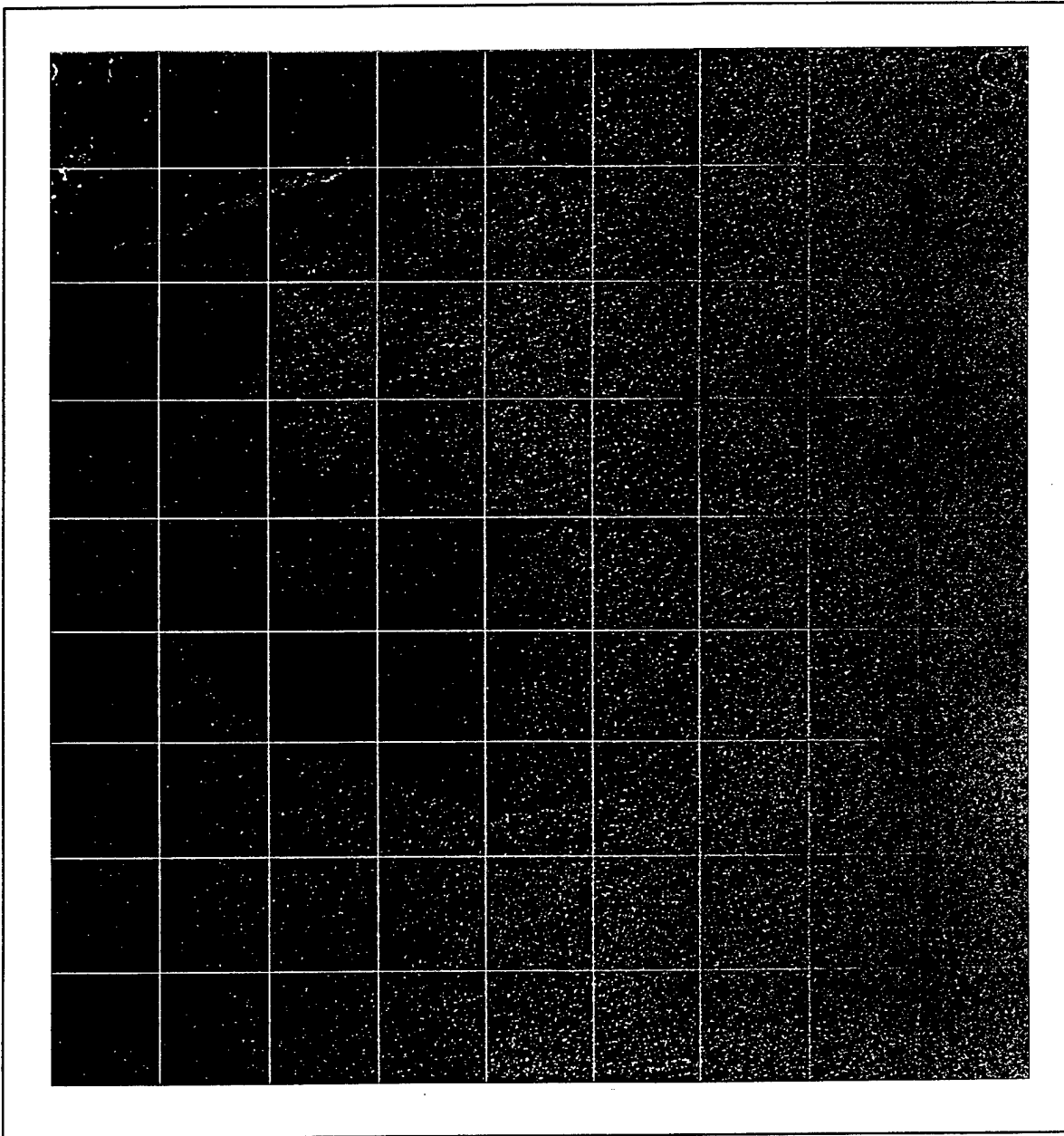


Figure 4.18 SAR Image Number One for 23 September 1995.



**Figure 4.19** SAR Image Number Two for 23 September 1995.

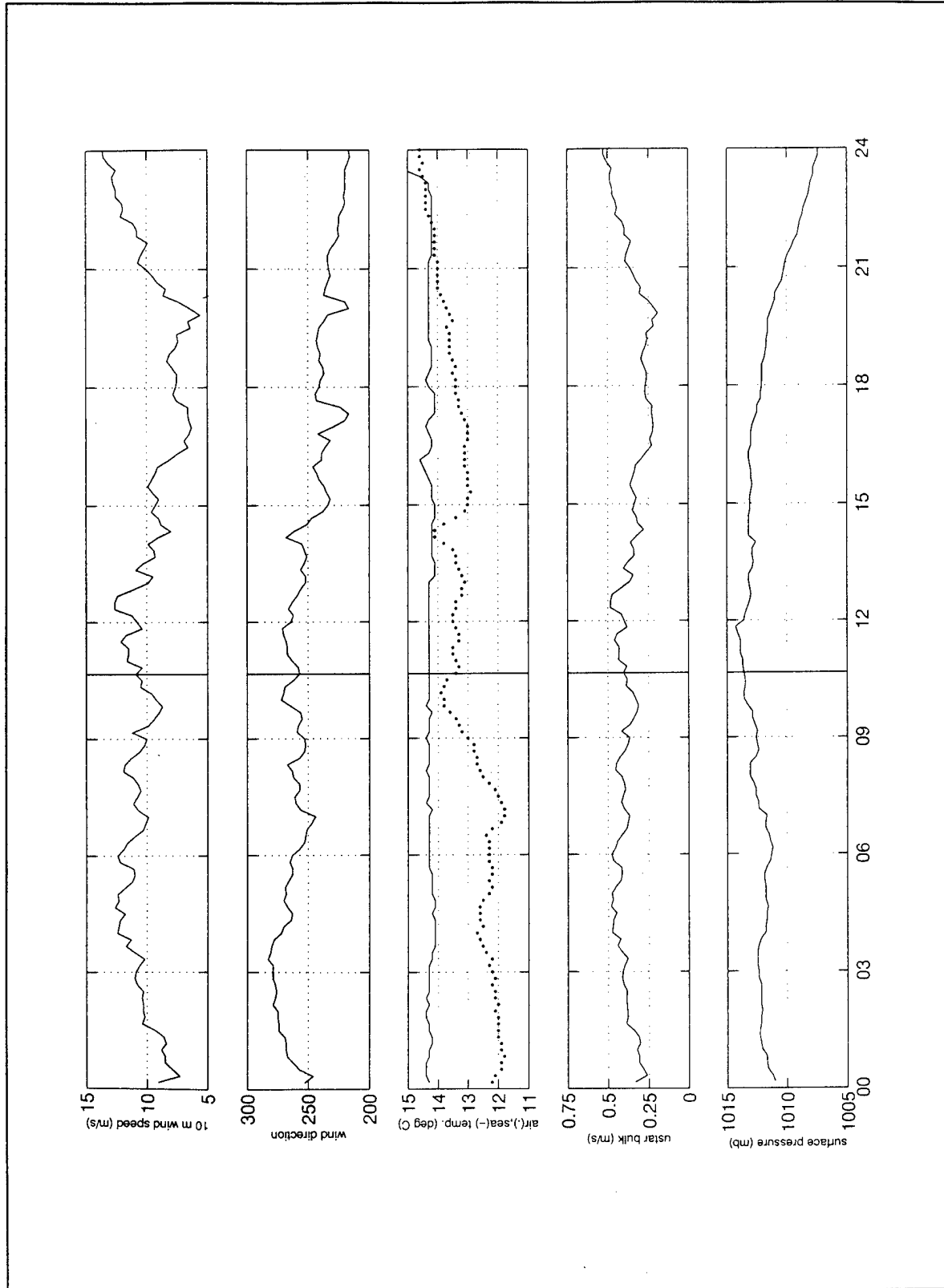


Figure 4.20 Time series of Meteorological Variables Measured on the R/V *Hakon Mosby* on 23 September 1995.

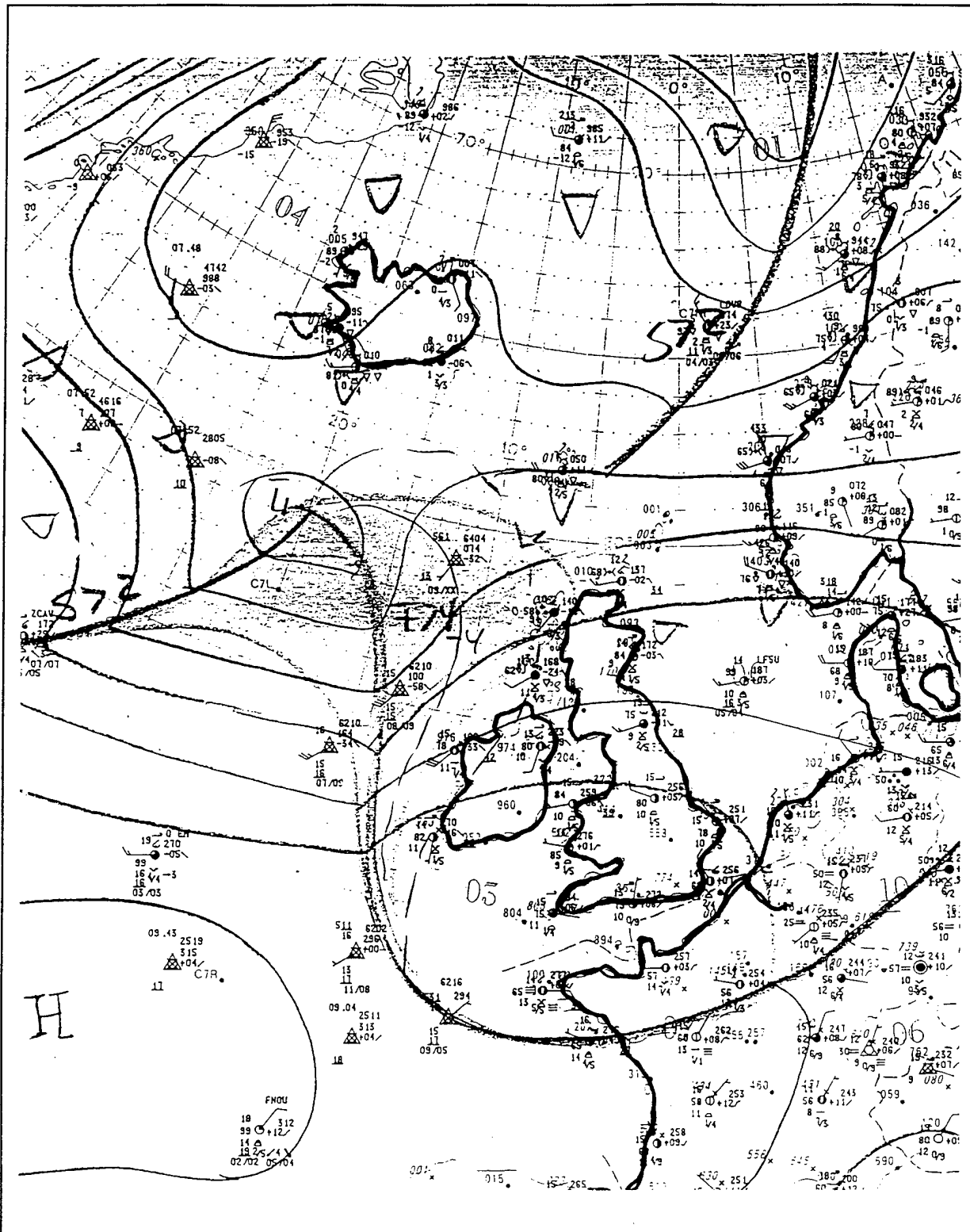


Figure 4.21 Surface Analysis for 0900 UTC 23 September 1995 Prepared by the Bergen, Norway, Western Norway Meteorology Center.



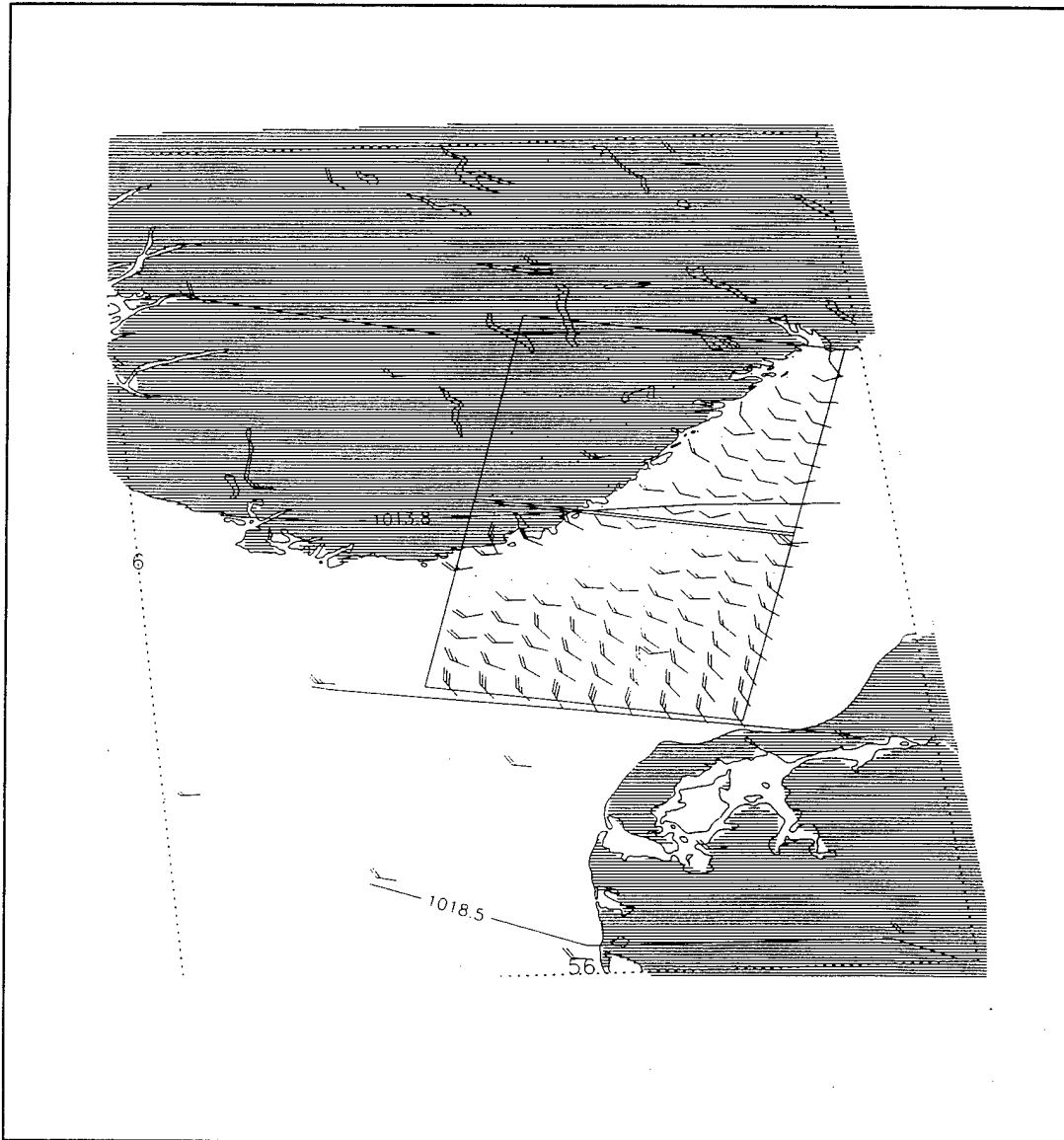


Figure 4.22 Combined Wind Vector Plot for 23 September 1995.

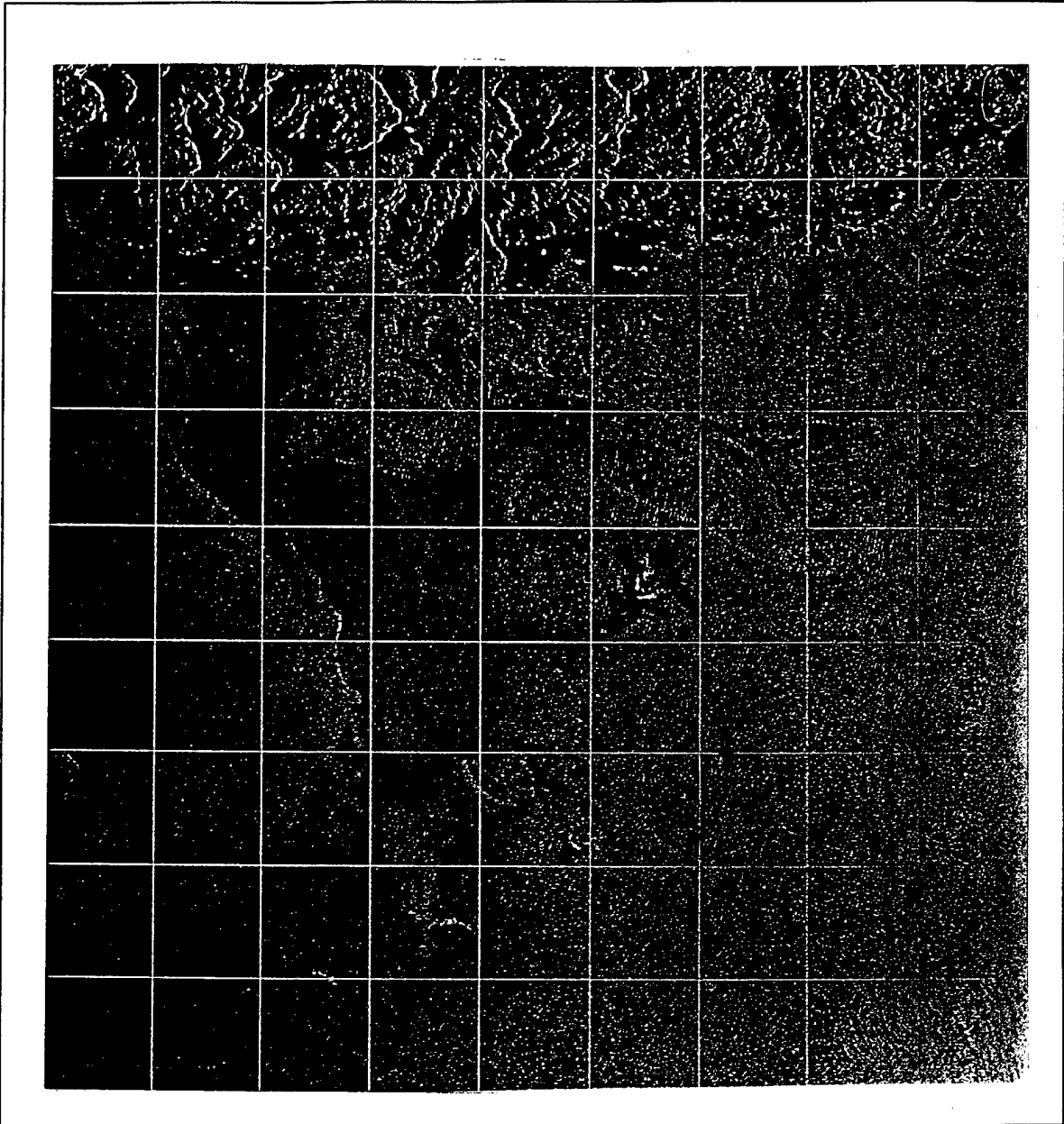
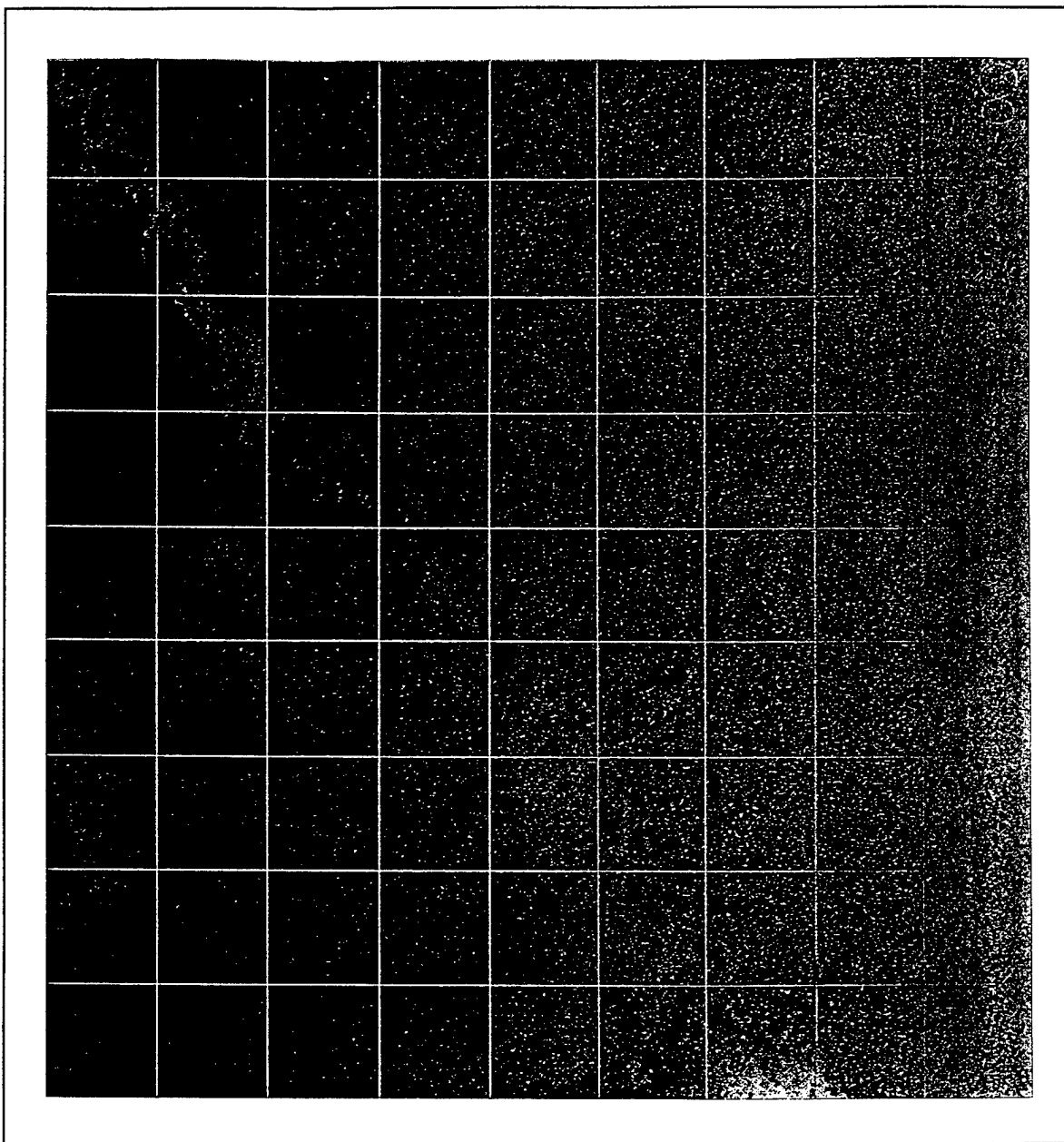
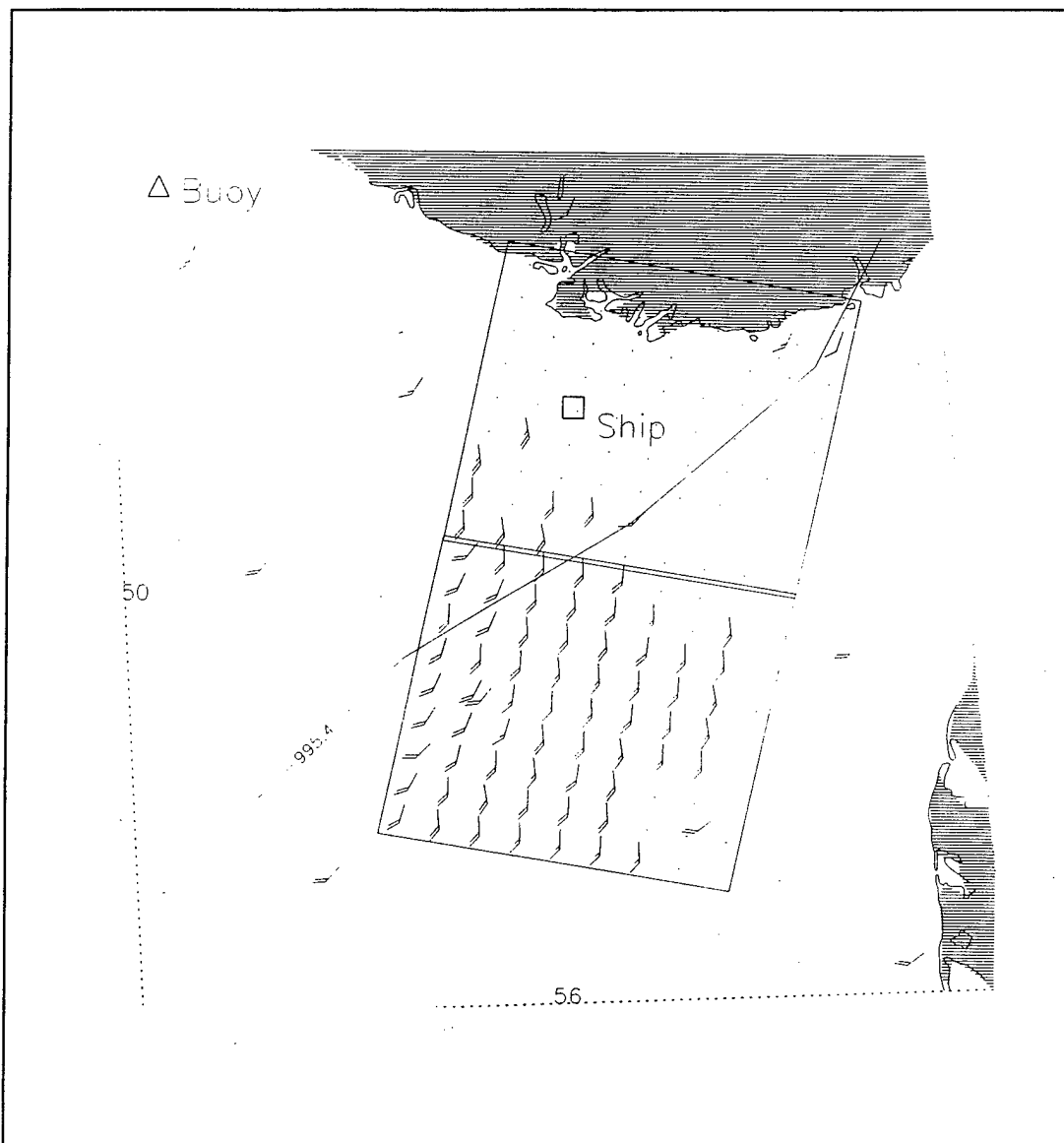


Figure 4.23 SAR Image Number One for 27 September 1995.



**Figure 4.24** SAR Image Number Two for 27 September 1995.



**Figure 4.25** Combined Wind Vector Plot for 27 September 1995

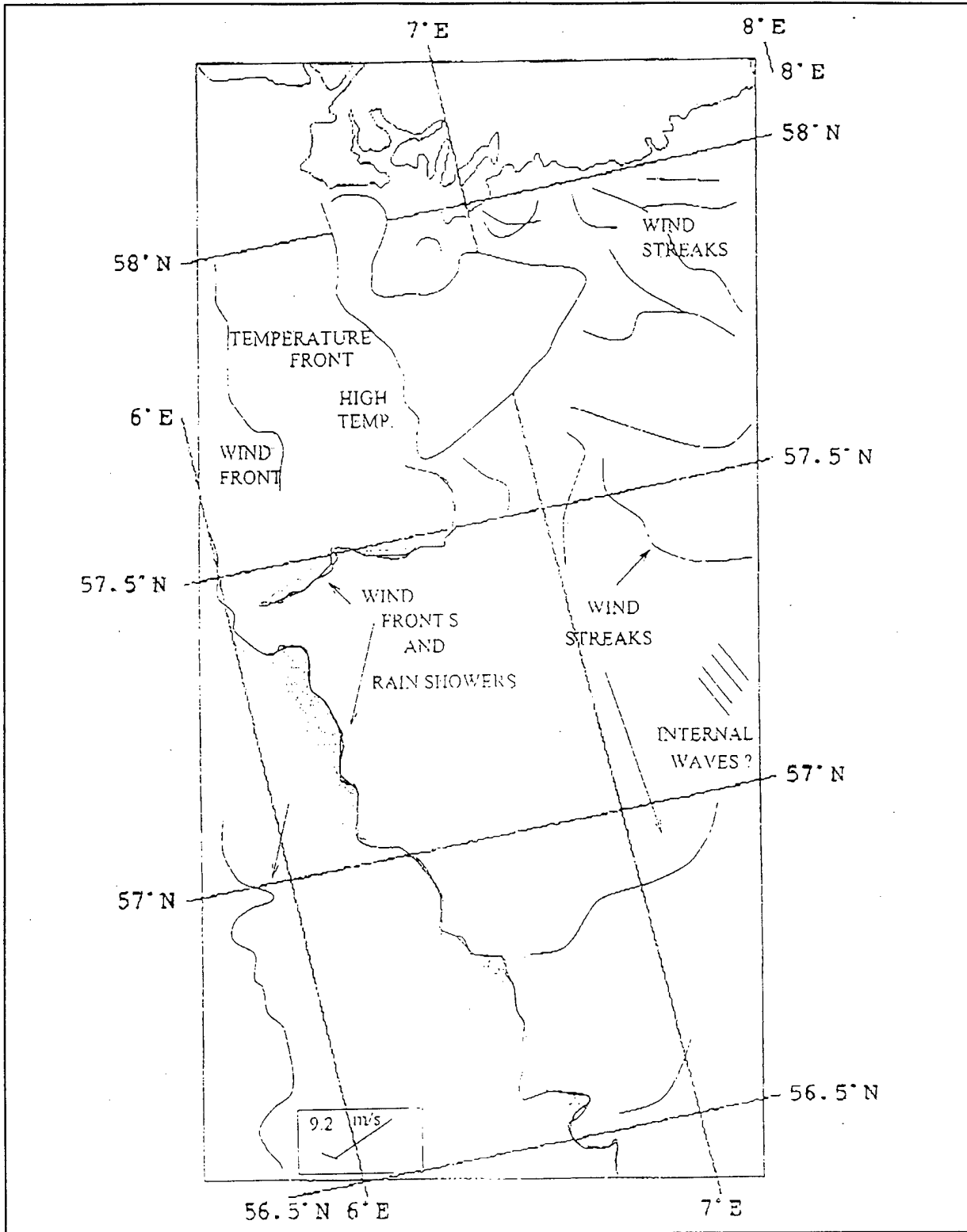


Figure 4.26 Preliminary Map Showing Location of SAR Features Analyzed from 27 September Images.



## V. CONCLUSIONS AND RECOMMENDATIONS

This thesis examined two SAR wind models used to evaluate ERS-1 and ERS-2 data from NORCSEX '95. As discussed in Chapter II, there were a total of fourteen satellite passes during the twenty days of NORCSEX '95. Four of these days (16, 17, 23 and 27 September) have been analyzed using the CMOD4 and SWA wind models. Of these four, the 16th and 17th were chosen to examine in the greatest detail since there were two sources of in-situ data (the R/V *Hakon Mosby* and the NPS buoy), available and the two models showed good agreement on the 17th and poor agreement on the 16th at the location of the buoy. However during the course of the thesis study it was discovered that the 16 September data used for the CMOD4 model was processed incorrectly and could not be used. If there had been time emphasis would have been placed on the 27 September data since the models had poor agreement at the location of the in-situ data. As I mentioned in Chapter IV, this data is being studied now.

Although based on different physical principles, the models returned similar results and were within 2 m/s of each other nearly 90% of the time. They also verified well with the in-situ measurements and showed good mesoscale resolution on the order of 10 km (Korsbakken 1996). The most difficult problem remaining in the application of the models is their automation. CMOD4, which is based on the relationship between surface wind stress (roughness) and SAR backscatter, requires a first guess wind that must be in the same general direction of the in-situ wind and an air-sea temperature difference for the stability correction. It also requires calibration for each image. Wackerman *et al.* (1996) have proposed a solution to the automation of the first guess wind direction for CMOD4 using windrows in the SAR images.

SWA is based on the modulation of ocean waves by the surface wind and has the advantage of requiring less calibration than CMOD4 but currently has no way of determining wind direction. The need for a stability correction in the SWA model has yet to be determined. The modulation of the ocean waves by the wind is very complex and is an area where further research is needed.

Korsbakken's combined wind vector approach increases the confidence level in the areas where the two models agree closely but retains the shortcomings of the individual models. Further validation of both models is needed to determine which is more accurate under the conditions where they diverge, and to determine what the accuracy of the models is under various weather conditions. Ultimately the automation problems must be solved to make SAR wind a useful tool to the military user.



## LIST OF REFERENCES

- Alpers, W. R., Ross, D. B., Rufenach, C. L., 1981: On the Detectability of Ocean Surface Waves by Real and Synthetic Aperture Radar, *Journal of Geophysical Research*, **86**, 6 481-6497.
- Alpers, W., and Hasselman, K., 1978: The Two-Frequency Microwave Technique for Measuring Ocean-Wave Spectra from an Aeroplane or Satellite, *Boundary Layer Meteorology*, **13**, 215-230.
- Allan, T. D., 1983: *Satellite Microwave Remote Sensing*, Ellis Horwood Limited, 526 pp.
- Beal, R. C., DeLeonibus, P. S., and Katz, I., 1981: *Spaceborne Synthetic Aperture Radar for Oceanography*, The Johns Hopkins University Press, 215 pp.
- Chapron, B., Fouhaily, T. E., and Kerbaol, V., 1995: Calibration and Validation of ERS Wave Mode Products, *IFREMER Document DRO/OS/95-02*, 32 pp.
- Curlander, J. C., McDonough, R. N., 1991: *Synthetic Aperture Radar, Systems and Signal Processing*, John Wiley and Sons INC., 647 pp.
- Edson, J. B., Fairall, C. W., Mestayer, P. G., and Larsen, S. E., 1991: A Study of the Inertial Dissipation Method for Computing Air-Sea Fluxes, *Journal of Geophysical Research*, **96**, 10 689-10 710.
- Hovanessian, S. A., 1980: *Introduction to Synthetic Array and Imaging Radars*, Artech House, Inc., 156 pp.
- Janssen, P. A. E. M., 1992: Experimental Evidence of the Effect of Surface Waves on the Airflow, *Journal of Physical Oceanography*, **22**, 12 234-12 298.
- Johannessen, J. A., Vachon, P. W., and Johannessen, O. M., 1995: ERS-1 SAR Imaging of Marine Boundary Layer Processes, *Earth Observation Quarterly*, ESA, **2**, 65-98.
- Komen, G. J., Cavaleri, L., Donelan, M., Hasselmann, S., Janssen, P. A. E. M., 1994: *Dynamics and Modelling of Ocean Waves*, Cambridge University Press, 532 pp.
- Korsbakken, E., 1995: Modelling and Analysis of Speckle Noise in A Synthetic Aperture Radar Ocean Imaging System, University of Tromso, NORUT Information Technology Ltd. 87 pp.
- Korsbakken, E., 1996: Quantitative Wind Retrievals From ERS SAR Images, European Space Agency, European Space and Technology Center, 81pp.
- Laur, H., Meadows, P., Sanchez, J. I., and Dwyer, E., 1993: ERS-1 Radiometric Calibration, Technical Report, ESA ESRIN Frascati, Italy, 64 pp.

Meadows, P. J., and Willis, C. J., 1995: Derivation of Radar Cross Section Coefficient in UK-PAF ERS-1 SAR PRI Products, Report GEC-MARCONI Research Center, 54 pp.

Napolitano, D. J., 1991: Synthetic Aperture Radar Measurements of the Ocean Surface During the Gulf of Alaska Experiment, Report D925-1991-1, 20 pp.

Scoon, A., 1995: Analysis and Interpretation of SAR Data for the English Channel, Thesis, Ph.D, University of Southampton, 63 pp.

Stofflen, A. And Anderson, D. L. T., 1993: ERS-1 Scatterometer Data and Characteristics and Wind Retrieval Skill, *Proceeding of the First ERS-1 Symposium*, ESA, SP-359, 57-75.

Taylor, W. R., Editor, 1981: *Spaceborne Synthetic Aperture for Oceanography*, The Johns Hopkins University Press, 215 pp.

Vachon, P. W. and Dobson, F. W., 1995: Validation of Wind Vector Retrieval from ERS-1 Images over the Ocean, submitted to *Global Atmosphere-Ocean System*, May 1995.

Vachon, P. W., Johannessen, J. A., and Brown, D. P., 1995: ERS-1 SAR Images of Atmospheric Gravity Waves, *IEEE Trans. Geoscience and Remote Sensing*, **33**, 1014-1025.

Wackerman, C. C., Rufenach, C. L., Shuchman, R. A., Johannessen, J. A., and Davidson, K. L., 1996: Wind Vector Retrieval Using ERS-1 Synthetic Aperture Radar Imagery, *Geoscience and Remote Sensing*, **34**, 1343-1352.

Wu, J., 1993: Ripples and Oceanic Remote Sensing, *Proceeding Environment '93 HKUST*, Hong Kong, 45-86.

## INITIAL DISTRIBUTION LIST

1. Defense Technical Information Center 2  
8725 John J. Kingman Road., Ste 0944  
Ft. Belvoir, VA 22060-6218
2. Dudley Knox Library 2  
Naval Postgraduate School  
411 Dyer Rd.  
Monterey, CA 93943-5101
3. Dr. Juergen Richter, Code 54 1  
Naval Command and Control and Ocean Surveillance  
Center, RDT&E Division (NRaD), 54  
San Diego, CA 92152-5000
4. Dr. Ola M. Johannessen 1  
Geophysical Institute, University of Bergen,  
and Nansen Environmental and  
Remote Sensing Center  
Edv. Griegs vei 3a  
N-5037 Solheimsvik, Norway
5. Erik Korsbakken 1  
Geophysical Institute, University of Bergen,  
and Nansen Environmental and  
Remote Sensing Center  
Edv. Griegs vei 3a  
N-5037 Solheimsvik, Norway
6. Dr. Kristina Katsaros 1  
IFREMER, Center de Brest  
BP 70, F-29280  
Plouzane, France
7. Dr. Bertrand Chapron 1  
IFREMER, Center de Brest  
BP 70, F-29280  
Plouzane, France

- |    |   |   |
|----|---|---|
| 8. | Professor K. Davidson<br>Meteorology Department, Code MR/DS<br>Naval Postgraduate School<br>Monterey, CA 93943-5002 | 2 |
| 9. | Professor C. Wash<br>Meteorology Department, Code MR/WS<br>Naval Postgraduate School<br>Monterey, CA 93943-5002     | 2 |
| 10 | LCDR James B. Hart<br>Naval Pacific Meteorology and Oceanography Center<br>Box 113<br>Pearl Harbor, HI 96860-5050   | 1 |